DOI 10.1007/s10812-014-9998-2
Journal of Applied Spectroscopy, Vol. 81, No. 5, November, 2014 (Russian Original Vol. 81, No. 5, September–October, 2014)

STANDOFF DETECTION OF HIDDEN EXPLOSIVES AND COLD AND FIRE ARMS BY TERAHERTZ TIME-DOMAIN SPECTROSCOPY AND ACTIVE SPECTRAL IMAGING (REVIEW)

L. A. Skvortsov

UDC 53.043;53.06

Terahertz time-domain spectroscopy and standoff spectral imaging for detection of explosives and cold and fire arms hidden, for example, under clothing, were reviewed. Special attention was paid to different schemes for practical implementation of these methods. Progress in this direction and existing problems and the prospects for their solution were discussed. Issues related to sources and receivers of terahertz radiation were briefly discussed. It was noted that interest in quantum-cascade lasers as compact sources of terahertz radiation and the potential of using them at room temperature were increasing.

Keywords: *terahertz time-domain spectroscopy, active spectral imaging, explosives, standoff detection, quantum-cascade laser.*

Introduction. The terahertz (THz) range of electromagnetic radiation is definitely of interest for applications such as high-frequency communications, ecological monitoring, quality control of medicines and foods, biological and medical diagnostics, and discovery of new directions, e.g., coherent THz-tomography and THz-ranging. The unique properties of THz frequencies acquire special significance for security problems, i.e., the detection of hidden explosives, narcotics, and cold and fire arms.

An analysis of laser methods for remote detection of traces of explosives [1–3] on surfaces would be incomplete without a discussion of time-domain THz-spectroscopy and active spectral imaging, the recent rapid development of which is related to the use of lasers. In particular, the significant number of articles and reviews, including those of Russian researchers, provides evidence of this [4–24]. Two different approaches to remote detection of explosives are known. The first is called standoff detection in the foreign literature. For this, inspectors and equipment are located at a safe distance from the inspection site (10–100 m). This detection method should be differentiated from the other type of remote explosives detection, so-called remote detection, where only the inspector is located at a safe distance. In the latter instance, a robotic platform with equipment is situated close to the suspect object. As a rule, contact-free detection is used in both methods.

The present review was limited to a discussion of only those issues that are directly related to the application of laser remote probing for counter-terrorism purposes, in particular, for detecting explosives and cold and fire arms hidden under a masking material. It is noteworthy that standoff applications [1] address not the detection of trace quantities of substances but the detection of mass explosives and devices in addition to cold and fire arms, e.g., those hidden under clothing or in bags or baggage. Special attention was paid to the application of THz quantum-cascade lasers (THz QCL) to solve the aforementioned problems, the progress achieved, and, in our opinion, the problems and prospects of solving them. Other laser methods for generating THz-radiation were briefly discussed. These were reviewed rather thoroughly in several reviews and articles [4–22]. The results obtained by the various methods were compared. Thus, laser methods for detecting traces of explosives and THz-spectroscopy and active imaging that are aimed mainly at the detection of hidden mass explosives and cold and fire arms are not only not competitive but, on the other hand, complementary in resolving essentially a single problem related to the security from and the prediction of terrorist activity.

It is commonly accepted that the THz-range covers frequencies from 300 GHz to 10 THz (1 mm to 30 μm in wavelengths) [5]. This is a significant range of electromagnetic radiation between the microwave and IR ranges (Fig. 1). The following properties of THz-radiation must first be noted [5, 7]. It is non-invasive and is not ionizing radiation. It does not present a hazard to human health at moderate intensities. It is scattered less than visible or IR radiation because

A. M. Prokhorov Academy of Engineering Sciences, 19 Presnenskii Val, Moscow, 123557, Russia; e-mail: lskvortsov@gmail.com. Translated from Zhurnal Prikladnoi Spektroskopii, Vol. 81, No. 5, pp. 653–678, September–October, 2014. Original article submitted October 9, 2013; final revision, June 18, 2014.

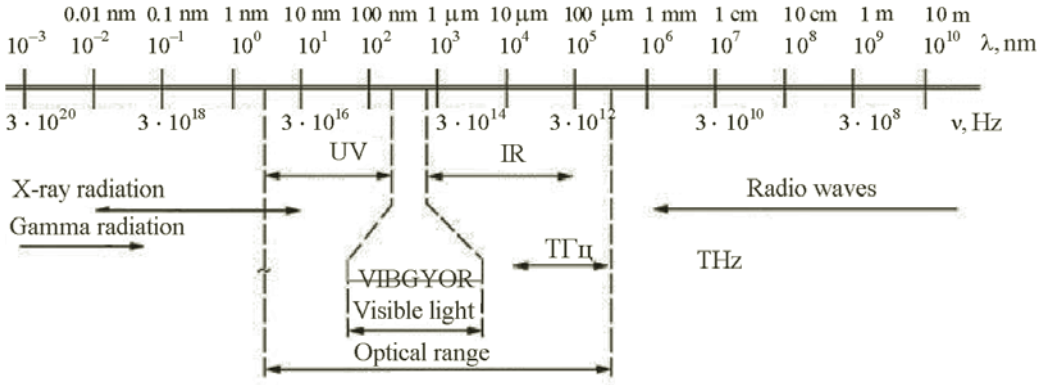

Fig. 1. Electromagnetic radiation scale [6].

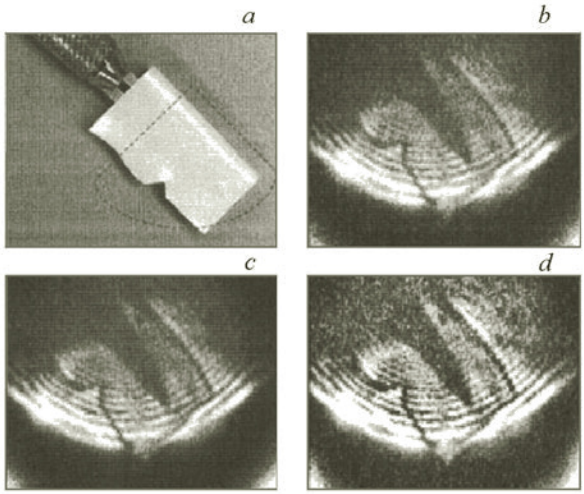

Fig. 2. Partial image of a knife in an opaque plastic package: usual digital photograph (dashed line, irradiated region) (a); single frame with image of knife blade obtained using a microbolometric camera with irradiation by a quantum-cascade laser at 2.7 THz (b); image of knife obtained by averaging 50 frames (c); image processed using the MATLAB program [23] (d).

it has a longer wavelength ($1/\lambda^4$). Therefore, objects such as dry cloth, wood, paper, and plastics are transparent in the THz-range (with the exception of metals and substances consisting of polar molecules, e.g., H_2O). The spectral properties (radiation absorption and reflection coefficients, dielectric permittivity, etc.) of various solids including explosives have characteristic features (fingerprints) in the THz- range. This enables these substances to be identified. Polycrystalline substances exhibit such features, as a rule, because of characteristic resonant vibrational frequencies of the crystal lattice (phonon modes). Both the shape and composition of an investigated object can be determined by identifying substances using spectral data in combination with THz-range spectral imaging.

The aforementioned properties of THz-radiation are especially important for security because people and baggage in airports, at checkpoints, etc. can be inspected in order to detect items hidden, e.g., under clothing with spatial resolution sufficient to identify them (~1 mm) and without health effects on the people being inspected. The same can be said of the application of this radiation to expose terrorists in large crowds. Figure 2 shows that THz-radiation is reflected well by metals due to their high conductivity, which provides a high-contrast image for detecting cold or fire arms hidden under clothing. It is shown below that an image of RDX (cyclotrimethylenetrinitramine), which is known as hexogen or cyclonite, and several plastic compounds based on it can be produced in high contrast if the object is irradiated at resonant frequency 0.82 THz. However, the contrast in this instance is achieved because of strong absorption at the resonant frequency in these objects.

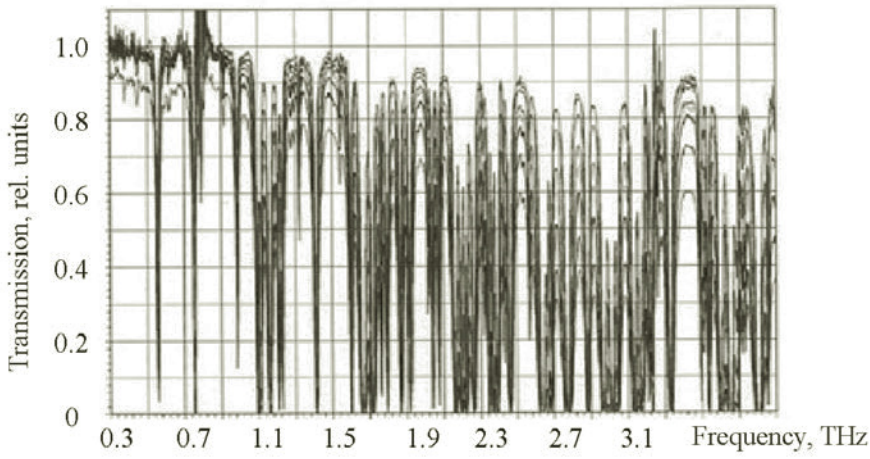

Fig. 3. Transmission of atmosphere in the THz region 0.3–4.0 THz (transmission at 0.3 THz is taken as unity) as a function of relative humidity measured at 5% (upper curve) up to 58% (lower curve) [24].

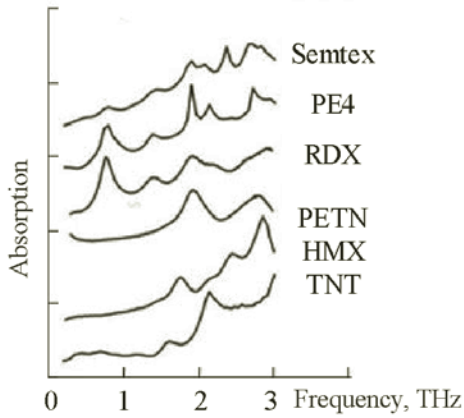

Fig. 4. Absorption spectra of several explosives (TNT = trinitrotoluene or trotyl; HMX = cyclotetramethylenetetranitramine or octogen; PETN = pentaerythritol tetranitrate or TEN) and their components (spectra are shifted vertically for clarity) [5].

Propagation of THz-Radiation in the Atmosphere. The effect of the atmosphere on standoff measurements is of fundamental significance. Figure 3 shows experimental measurements of the transmission of the atmosphere in the frequency range 300 GHz to 4 THz. Many absorption lines from various gaseous air components, in particular, water vapor, are found in the THz-range. Namely its effect limits significantly the capabilities of THz-spectroscopy for standoff measurements, including the highly variable line intensities for water-vapor absorption because of varying humidity. However, several windows in which the signal-to-noise ratio (SNR) can reach 50 dB and greater exist at distances up to several tens of meters, which are interesting for active standoff detection. This means that the atmosphere in these windows at moderate humidity and at relatively small distances (50–100 m) can be considered transparent enough for detecting hidden objects. Figure 3 shows that at least five different transmission windows in the range 1.4–4 THz exist in the atmosphere. These windows are centered around the frequencies 1.488, 1.979, 2.11, 2.52, and 3.42 THz. The windows at 2.11, 2.52, and 3.42 THz are well suited for existing THz-QCL (even experimental ones). Figure 4 shows that resonances of most explosives are located outside these windows so that their detection at long distances is hindered by atmospheric humidity >52%. However, RDX and plastic compounds based on it (Semtex, PE4, etc.) could be successfully detected at significant distances using radiation with frequencies near 0.9, 1.488, and 1.979 THz.

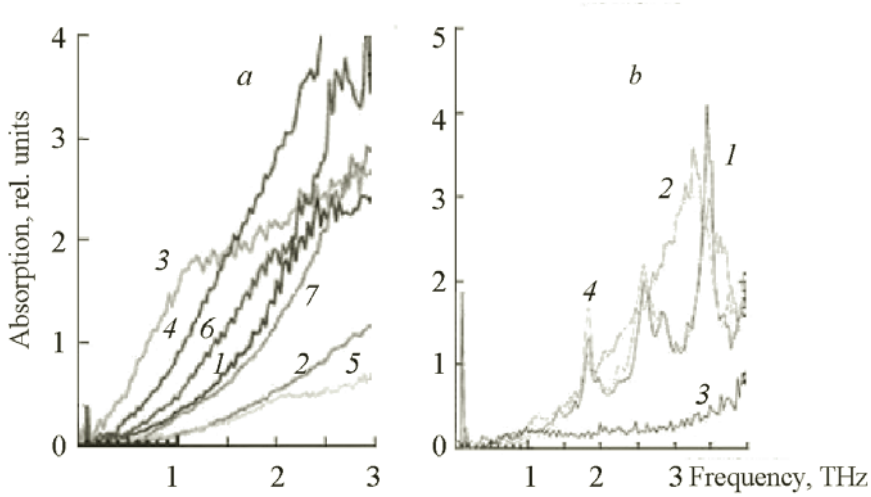

Fig. 5. Absorption spectra of materials: used to package and sew clothing (cotton, 1; silk, 2; wool, 3; leather, 4; nylon, 5; polyester, 6; polyester/cotton, 7) (a); capable of interfering with explosives identification (milk chocolate, 1; vitamins, 2; granulated sugar, 3; powdered sugar, 4) [5].

Fabrication of THz-QCL emitting at longer wavelengths and including the ranges 1.6–1.8 THz [25] and 1.2–1.6 THz [26] was reported. The windows near 2.11, 2.2, and 3.42 THz were entirely acceptable for standoff measurements up to relative humidity of 52%. However, problems with making standoff measurements could arise at higher humidities. Figure 3 also shows that the windows near 1.488 and 1.3 THZ present the best conditions for standoff detection. Windows at longer wavelengths of the THz-range are even more attractive for standoff applications. However, they are now accessible for QCL only in the presence of a magnetic field [27].

Spectral Features for Detecting Explosives in the THz-Range. Many substances exhibit rather pronounced spectral features in the submillimeter wavelength range of 0.1–1 mm (from 300 GHz to 3 THz) although they are less than in the mid-IR range [1–3]. Explosives are polycrystalline in the solid state. Therefore, intermolecular and crystal-lattice vibrations are the basic contributors to the spectral features of explosives (resonances) in the THz-range [28]. THz-spectra for the absorption of several materials have been reported [28–31].

Both transmission and reflectance (total or diffuse) spectra of THz-radiation can be measured. A geometry allowing THz-radiation diffuse reflectance spectra of an object to be measured is the main version used for standoff detection. Thus, the emitter and receiver are located on the same side of the target. This is especially important for bulky objects in which absorption of the radiation would be significant. Spectra of explosives obtained in various geometries and for various objects and frequency ranges were reported [32–41]. The absolute absorption cross sections of several explosives (TNT, RDX, HMX, and PETN) at resonant frequencies were published [42].

Figure 4 shows absorption spectra of several explosives and their components [5]. It can be seen that they all exhibit features specific to each material. For example, explosives based on RDX (PE4, Semtex) have near 820 GHz a distinct peak (resonance) that enables these substances to be identified. However, features in the absorption (reflectance) spectrum are a necessary but not sufficient condition for identifying an unknown substance. It is important that spectra of other materials that are non-hazardous and have similar features can be distinguished from spectra of explosives. This condition is fulfilled in the THz-range for practically all non-explosive materials that are routinely encountered (Fig. 5a) [5, 43–45]. However, materials that interfere with explosives detection exhibit spectral features that differ considerably from those of explosives (Fig. 5b). This means that their effects are easily removed. This distinguishes favorably the THz-range from the mid-IR range, in which the situation is more complicated [1]. The range up to 6 THz or even 10 THz is characterized by a large number of spectral features for explosives [7, 34, 46]. However, as noted earlier, humid air is opaque for radiation in the range >2–3 THz [47]. Therefore, the comparatively narrow portion (0.3–3 THz, 0.1–1 mm) of the THz-spectrum, the so-called submillimeter range, is considered the best for standoff applications.

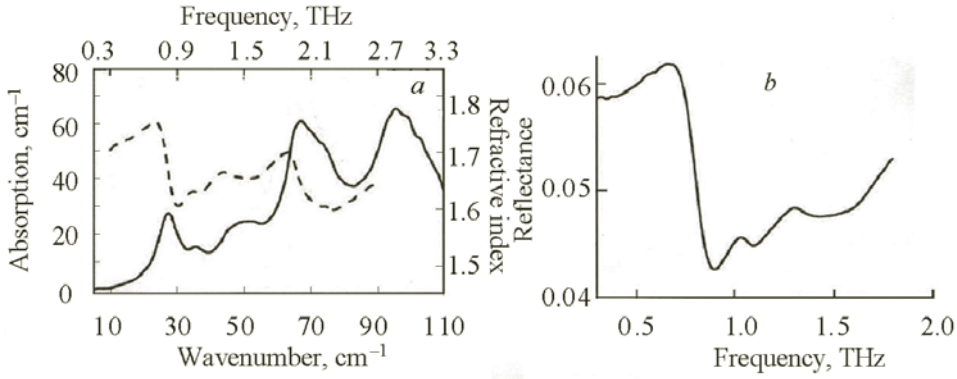

Fig. 6. Absorption coefficient (solid line) and refractive index (dashed line) as functions of THz frequency for Semtex-H obtained using transmission spectroscopy (a) and calculated spectral dependence of reflection coefficient (b) [5].

As a rule, standoff detection of objects in the THz-range records back-scattered radiation. However, the spectral dependences of the absorption coefficient $\alpha(\omega)$ and refractive index $n(\omega)$ are usually measured in transmission mode. Figure 6a shows them for Semtex-H as an example. The refractive index $n(\omega)$ and absorption coefficient $\alpha(\omega)$ in the THz-range are calculated using the measured amplitudes and phases of radiation passing through the sample and the expressions [20]:

$$\alpha(\omega) = \frac{2}{d}\left\{-\mathrm{Re}\left(\ln\frac{E_{tr}(\omega)}{E_0(\omega)}\right) + \ln\frac{4n(\omega)}{\left(n(\omega)-1\right)^2}\right\}, \tag{1}$$

$$n(\omega) = 1 + \frac{c}{\omega d}\mathrm{Im}\left(\ln\frac{E_{tr}(\omega)}{E_0(\omega)}\right). \tag{2}$$

Here, $E_0(\omega)$ and $E_{tr}(\omega)$ are the radiation electric field strengths before and after transmission through the sample; d, the sample thickness; ω, the radiation frequency; and c, the speed of light. It is noteworthy that knowledge of the functions shown in Fig. 6 provides a basis for converting the measured transmission spectra into reflectance spectra [20, 30]. In fact, the $n(\omega)$ value determined from the transmission spectroscopic data enabled reflectance coefficient $R(\omega)$ to be determined approximately using the formula [20]:

$$R(\omega) \approx \left(\frac{n(\omega)-1}{n(\omega)+1}\right)^2, \tag{3}$$

where $n(\omega)$ is the spectral component of the substance refractive index. Figure 6b shows the spectral dependence of the reflectance coefficient for Semtex-H that was calculated using Eq. (3).

Figure 7 shows the measured and calculated spectral reflectance functions of Semtex-H [5, 20]. It can be seen that the curves agreed well. The characteristic features of the calculated reflectance coefficient function obtained from transmission data were also observed for the measured Semtex-H reflectance as a function of frequency. According to the researchers [7, 20, 30, 45], the results of the spectral studies indicated that hidden substances and items could be detected using standoff searches that recorded their diffuse-scattered radiation and that they could be identified using time-domain THz-spectroscopy. According to the researchers [5, 7, 30, 45], the previous spectral results suggested that hidden substances and items could be detected by recording their diffuse-scattered radiation and that they could be identified using time-domain THz-spectroscopy. However, it is noteworthy that measurements of the spectral characteristics did not take into account that scattering of the radiation at medium non-uniformities contributed greatly to the overall spectral attenuation coefficient of the material for THz-radiation. Scattering is complicated depending on the medium structure and distorts significantly the recorded spectral characteristics of the object if the sizes of the non-uniformities in the material are comparable to the radiation wavelength.

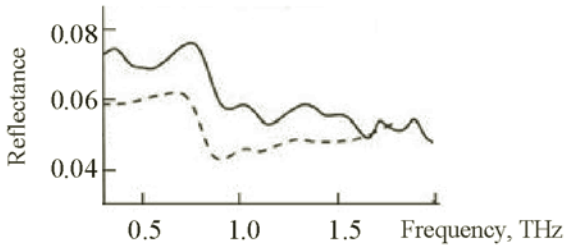

Fig. 7. Measured (solid curve) and calculated (dashed curve) spectral dependence of Semtex-H reflectance [5].

The search for and identification of explosives from their THz-spectral characteristics could be hindered because the substance itself and the packing materials are scatterers. The search for hidden arms using THz-imaging systems could also be complicated by scattering from clothing. Scattering by fibers of such materials can substantially reduce the image contrast of a hidden object. Obviously, scattering of THz-radiation in various media must be investigated during the development of THz-systems for the search for and identification of hidden items.

Experimental and theoretical studies of THz-radiation scattering by clothing and packing materials have not yet been conducted. The experimental measurement of scattering characteristics causes difficulties because specialized expensive devices must be developed. One possible way to study THz-radiation scattering in packing materials is mathematical modeling [4].

Principal Types of THz-Radiation Sources and Receivers. Until recently, the THz-range was a poorly studied region of the electromagnetic spectrum (THz-gap). The main reason for this was the lack of compact and rather powerful (>100 mW average power) solid-state sources of coherent THz-radiation and sensitive receivers for recording it. As noted, the THz-range is located between the microwave and IR ranges of the electromagnetic spectrum, for each of which well-developed semiconducting radiation sources are available. However, the construction principles of these devices are completely different. Microwave electronic devices (e.g., UHF transistors and Hann diodes) are based on electron transport by charge carriers. Therefore, the upper operating frequency of classical electronic devices depends on the time of flight of a charge carrier between the electrodes and a time constant determined by the parasitic device RC-parameters. The power level of classical microwave devices decreases with emission frequency as $1/f^4$ and even faster when the frequency is >1 THz [24]. The last condition limits in principle the application of such devices to standoff and other important applications that require mastery of the THz-range.

Devices operating in the visible and IR ranges (lasers) are based on quantum-mechanical principles, i.e., transitions between active energy levels and stimulated emission effects. A required condition for laser operation is the population inversion of the energy levels. The mean thermal excitation energy ($\sim kT$) has a defining influence on this. Thus, the low energy of THz-radiation quanta (a frequency of 1 THz corresponds to $T = 47.6$ K or 4.14 meV) is comparable to the thermal excitation of $\sim kT$, which equilibrates the populations in the inversion medium. This limits the application of optical technologies in this spectral range. It also makes the use of photonics principles problematic for fabricating solid-state (semiconducting) THz-systems that operate at room temperature. A problem just as serious arises in fabricating a THz-radiation quantum detector operating at room temperature and is related to the environmental thermal background that limits significantly the detector threshold characteristics.

Relaxation of the population inversion as a result of thermal excitation is less effective in other THz-radiation sources. These include molecular gas lasers (MeOH) with optical pumping by a CO_2-laser or electronic-vacuum devices that use the movement of electrons in electric and magnetic fields (reverse wave lamps and gyrotrons). They require high-voltage power sources, have large footprints, do not exhibit the required spectral and power characteristics, and cannot be smoothly tuned in the THz-range. Also, unique devices such as free-electron lasers or synchrotrons are based on charge transfer and can supply rather powerful THz-radiation. However, they are very expensive and massive so that they cannot be used to solve the aforementioned problems.

The problem of practical implementation of the unique capabilities of the THz-range was solved relatively recently and was possible owing to the fabrication of THz-sources based on the action of laser radiation on a substance

(optical-terahertz transformation) [5–9, 14, 20]. Methods based on the transformation of energy from the optical range into the THz-range (during generation) and back (during detection) were developed during the last decade. Such transformation is effected in general in two ways. These are optically induced linear charge-carrier generation processes in photoconductive semiconductors that are accompanied by subsequent emission of THz-radiation by accelerated charges and nonlinear optical parametric frequency shift processes [48–53]. The first group of devices, semiconducting photoconductive antennae, which we will examine separately, are used most often. With respect to the second group of devices, THz-radiation in nonlinear-optical crystals is generated mainly by optical rectification of ultra-short femtosecond laser pulses. THz-radiation can be produced during propagation of a femtosecond pulse through a nonlinear crystal of a given symmetry and composition as a result of coherent beating of the pulse frequency components. Some of the best results in this respect were obtained by pumping lithium niobate ($LiNbO_3$) crystals with Ti:Sa femtosecond laser pulses with a beveled intensity front. For this, the optical-terahertz conversion coefficient reached the record value of 10^{-3} for a laser repetition rate of 100 Hz, which corresponded to a THz-pulse energy of 30 μJ [53]. Highly sensitive systems for THz-radiation detection for this instance use most often a dynamic Pockels electro-optic effect. The incident THz-pulse changes the crystal refractive index because of the electro-optic effect. The change of refractive index is detected because the optical detecting radiation changes polarization as it passes through the crystal with a time delay relative to the THz-radiation [5–8, 20, 54]. Nonlinear crystals of GaAs (LT-GaAs), DAST (dimethylaminosulfur tetrafluoride), GaP, ZnTe, CdTe, and $LiNbO_3$ are used for both generation and detection [7, 12, 13, 15, 55–58] because they have low absorbance and high nonlinear susceptibility in the THz-range. The best optical-terahertz energy transformation efficiencies that have been achieved today are low and have approximately the same value of ~0.1% [6, 59]. On one hand, this is the main reason for their limited application and, on the other, for the search for new coherent THz-radiation sources.

In addition to laser detection methods [60, 61], a large variety of THz-detectors includes Schottky diodes operating at room temperature, bolometers based on Bi or Te compounds, and Golay cells (opto-acoustic transformers). Cooled bolometers based on a Ge–Si system and composite bolometers based on a superconductor:insulator:normal metal tunneling transition were demonstrated. Their noise-equivalent power (NEP) was from $3 \cdot 10^{-17}$ to 10^{-18} $V \cdot Hz^{-1/2}$ [24]. A superconducting hot-electron bolometer for the far-IR range 30–300 μm with a NbTiN transition-edge sensor (TES) fabricated on a sapphire substrate was reported [62]. The superconducting bolometer reached NEP sensitivity level $3 \cdot 10^{-19}$ $W \cdot Hz^{-1/2}$, which was close to its value for an ideal photon detector (NEP = 10^{-20} $W \cdot Hz^{-1/2}$). The noise was limited to unremoved schrot noise due to background cosmic microwave radiation. Nevertheless, the researchers hoped to improve the results by decreasing the sensor physical dimensions.

Quantum-cascade lasers (QCL) represent a new class of promising THz-radiation sources [63–92]. Rapid depletion of the final states of emitting inter-level transitions in the active quantum well is required to operate this type of lasers. The characteristic time of non-radiative transitions to the ground level should be greater than the ground state depletion time in order to create a population inversion during operation in the THz-range. The characteristic inter-level transition times and the ground-state depletion time in $A^{III}B^{V}$ semiconductor heterostructures are determined by scattering of "hot" electrons at longitudinal optical (LO) phonons (phonon channel of carrier cooling) [27]. Bartel et al. fabricated one of the first THz-QCL based on AlGaAs/GaAs heterostructures in which the ground level was depleted by LO-phonons [92]. The THz-QCL was constructed of many waveguides extracting the THz-radiation from the multi-layered crystal active region because of its strong absorption in it [27].

Modern THz-QCL can operate in the frequency range 1–5 THz. Their radiation power in CW mode reaches >100 mW at cryogenic temperatures [27]. It is noteworthy that the output power of a QCL depends strongly on the pump current. Figure 8 shows the output power as a function of current for a QCL with a highly reflective rear-face coating. It can be seen that the peak QCL power in pulsed mode exceeded the symbolic value of 1 W at 10 K for emission frequency 3.4 THz [66]. Furthermore, the laser radiation became multi-modal and its spectrum broadened and shifted to higher frequencies as the current density increased.

The THz-QCL generation line width with distributed feedback (DFB) was only several tens of kHz. This made them ideal devices for use as local generators for heterodyne detection. It is important that local generators be tunable over frequency. Various methods are known for tuning THz-QCL frequency. Most systems use an external cavity with a diffraction grating for this [27, 89, 90]. However, the tuning range is less than ~10% of the central frequency.

It is now experimentally demonstrated [75] that inter-level and inter-subband elastic scattering (at dopants and ruffled heterojunctions) is significantly suppressed in a quantized magnetic field because of the large distances between Landau levels. Generation at 3 and 1 THz at 225 and 215 K in magnetic fields of 19.3 and 31 T was produced [75]. Also, a

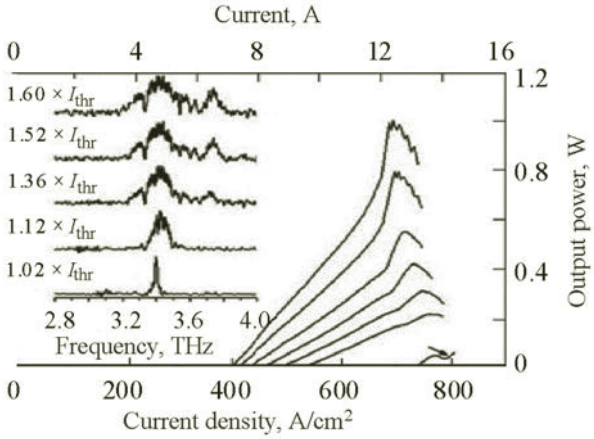

Fig. 8. Output power as a function of current for QCL with a highly reflective coating on the rear face; in the inset, spectral composition of laser radiation as a function of current density [66].

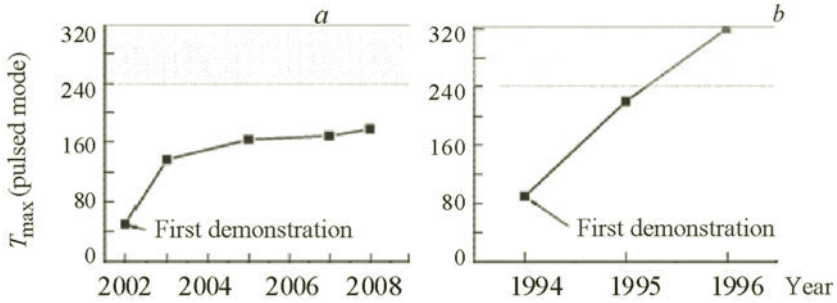

Fig. 9. Plots of yearly change of maximum operating temperature T_{max} (K) starting with the first demonstration of a QCL: THz frequency range (a) and mid-IR range (b).

record range of frequency change 0.68–3.38 THz was obtained for one laser. This corresponded to a maximum generation wavelength of 0.44 mm and justified the ability to use low-frequency atmospheric windows for THz-QCL.

The most important requirement for any semiconducting device is operation at room temperature. Until recently, this was unattainable for THz-QCL using traditional generation inversion diagrams in resonant-tunneling structures with quantum wells. Figure 9 shows a diagram illustrating the change of maximum operating temperature T_{max} over years starting from the first demonstration of a QCL. It can be seen that use of the traditional technology based on GaAs/AlGaAs heterostructures led to only a slow increase of operating temperature. Nevertheless, the slow increase of operating temperature suggests that the THz-QCL operating temperature will approach 250 K in the near future due to construction improvements based on compact thermoelectric coolers [77, 83].

However, not only in our opinion but in that of others [27, 74], fundamental changes in the traditional approach are needed in order to reach ambient operating temperatures. An alternative resolution of the situation involves developing generation diagrams without inversion and not creating a population inversion of closely spaced inter-band levels. The THz-radiation in them is created by the quadratic nonlinearity of the semiconducting structure owing to separation of the frequency difference $\omega_{THz} = \omega_1 - \omega_2$ upon mixing the two fields at frequencies ω_1 and ω_2 [73].

A similar nonlinear optical coupling that was insensitive to temperature and could be produced in several semiconducting crystals with strong nonlinear second-order susceptibility $\chi^{(2)}$ was examined [91] and led to difference frequency generation (DFG). THz-generation at room temperature with resonant amplification of DFG in the QCL active region in the mid-IR range was demonstrated [67]. The emission power was insignificant at ~0.3 μW. However, according to the researchers, the THZ-radiation power drop that was observed with increasing temperature was entirely due to a decrease of the pumping power in the mid-IR range whereas the efficiency of the DFG-transformation itself remained constant as the temperature rose. According to the researchers [27, 74, 91], many possibilities exist for improving the DFG-transformation

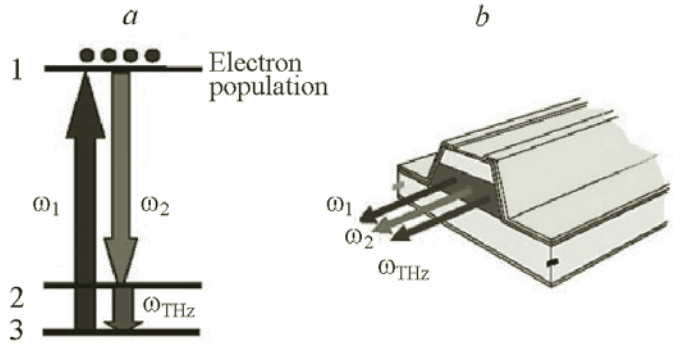

Fig. 10. Schematics of difference frequency generation (DFG) (a) and THz-radiation source based on intracavity DFG in the medium of a dual-wave QCL in the mid-IR range with frequencies ω_1 and ω_2 (radiation at terahertz frequency ω_{THz} is generated by DFG) (b) [73].

efficiency. Therefore, milliwatt THz-radiation powers at room temperature should be achieved in the near future. Figure 10 shows a schematic of a THz-radiation source operating on the DFG principle.

Several publications confirmed this [68–71]. Thus, room-temperature THz-sources based on Cerenkov phase-matched DFG in dual-wavelength mid-IR QCL were reported [71]. Giant optical nonlinearities originating from inter-subband transitions provided an optical THz-conversion efficiency with non-collinear phase synchronism of ~70 $\mu W/W^2$, which was an order of magnitude greater than previously obtained values. Moreover, a THz-QCL that was also based on Cerenkov phase-matched DFG for a dual-wavelength mid-IR QCL was developed [72]. However, fundamental changes were made in the laser construction that resulted in the emission power of a single-mode laser operating at room temperature at 3.5 THz being 0.215 mW. The researchers intend to tune a CW laser to the range 1–4.6 THz in the near future [72].

Methods for generating THz-radiation in the atmosphere are being actively developed [93–97]. Several reasons are responsible for this interest. First, devices for transforming laser radiation into THz-radiation are not required. THz-radiation is generated in the atmosphere as a result of laser breakdown of air by the simultaneous action of the principal Ti:Sa laser radiation and its second harmonic, i.e., during generation of a plasma, the formation threshold of which for air is much greater than its value for photoconductive structures. Generation of THz-radiation by the combined pulses of fundamental and doubled frequencies was explained basically as the result of four-wave nonlinear optical rectification (a special case of four-wave coupling for which a quasi-constant field, the null harmonic, was generated). However, it was discovered subsequently that this phenomenon had a somewhat different physical mechanism. Without going into the details, we note that ionization played a key role in the generation of the THz-radiation [94, 97]. The limitation on the intensity of the laser radiation for the examined method was in fact lifted. Second, an important advantage of this method was the ability to generate and detect a broad and continuous spectrum of THz-radiation. Finally, THz-radiation can be generated in the immediate vicinity of a studied object for remote detection. This should increase the detection distance because the influence of absorbing water vapor is sharply decreased.

Nevertheless, several drawbacks typical of this method must be noted. The presence of plasma emission in the atmosphere deprives the method of a stealth factor, which can be unacceptable for several long-distance detection problems. The method is sensitive to external interferences such as atmospheric chemical pollution that can scatter the air breakdown thresholds and, correspondingly, the intensity of the generated THz-radiation. However, in our opinion, the main drawback of this method is the high-intensity laser radiation that is a definite hazard to people. The probability of damaging an object always exists, especially at large distances from it, because of the proximity of the breakdown site to its surface. It is improbable that this explosives detection method will be used in the presence of people and several other objects, the damage of which is unacceptable. However, problems in which objects can be damaged during inspection do exist.

The method under discussion has much in common with the remote filament-induced breakdown spectroscopy (R-FIBS) technology that was reported earlier [3] and is based on application of so-called filamentation, where a laser beam is divided into several plasma threads upon focusing a femtosecond pulse in the atmosphere. It was shown [97] that plasma threads created in the laser-radiation channel are also sources of THz-radiation. With respect to the application of this technology to the remote detection of explosives, only a few studies were reported [93, 95]. Thus, the ability to detect explosives at a distance of ~17 m was demonstrated [93]. However, it would be premature to consider practical use of this

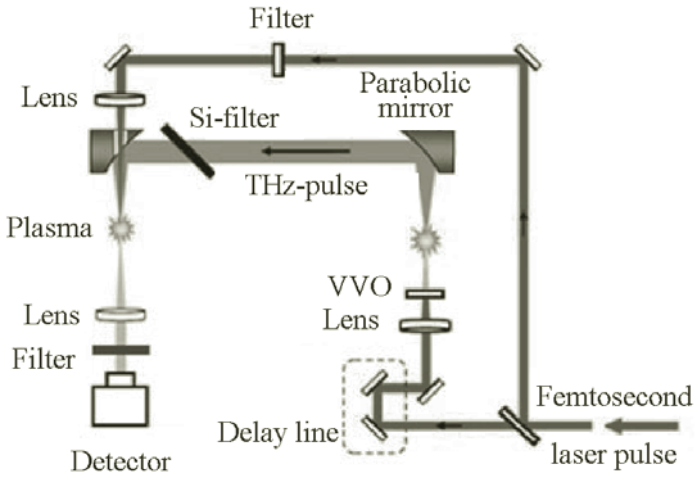

Fig. 11. Diagram of experimental set up for generation and detection of THz-radiation in the atmosphere [94].

TABLE 1. Comparison of Methods for Generating Terahertz Radiation

Method characteristics	Molecular lasers with optical pumping	Time-domain spectroscopy (THz TDS)	Direct multiplication of external generator frequency	Non-linear optical mixing of near-IR laser frequencies	THz-QCL (cryogenic temperatures) [66]	THz-QCL (cryogenic temperatures) [27]	THz-QCL (room temperature) [72]
Mean radiation power	>100 mW	~1 μW	mW–μW	<1 μW	1W (T = 10 K); 420 mW (T = 77 K) at 3.4 THz	>100 mW at 3–4 THz	0.215 mW
Frequency region	0.3–10 THz	0.1–2 THz	0.1–1 THz	0.3–10 THz	Depends on current structure and density	1–5 THz	1–4.16 THz (planned)
Tuning ability	Discrete frequency set	no	10–15% of central frequency	yes	yes	8–15% of central frequency (~300 GHz)	yes
Operating mode	CW/pulsed	pulsed	CW	CW	pulsed	CW/pulsed	pulsed

technology for standoff detection of explosives because the method is in the initial development stage. Figure 11 shows a diagram of a typical experimental set up for generating and detecting THz-radiation in the atmosphere.

In conclusion, Table 1 compares characteristics of the principal methods for generating THz-radiation. The data (without the QCL) were borrowed partially from the literature [8]. It was noted earlier that a THz-QCL with a broad smooth tuning range and a long-wavelength limit of 0.44 mm could be fabricated in a magnetic field. Therefore, it can be concluded based on the data in Table 1 and the development schedules of each method and the prospects for their further development that an effective solid-state THz-radiation source operating at room temperature and having a CW power generation mode of

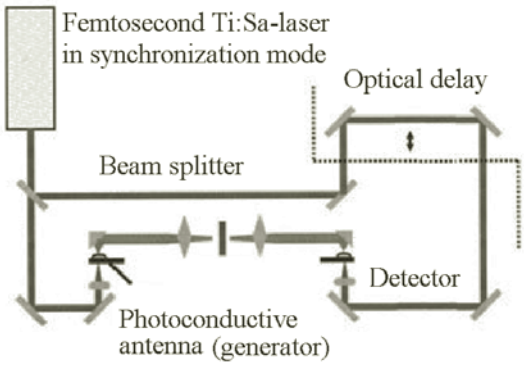

Fig. 12. Schematic of standard terahertz TDS-spectrometer for measuring transmission [8].

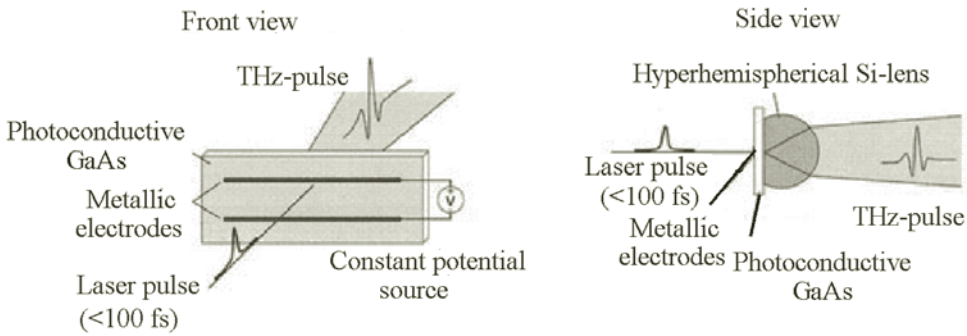

Fig. 13. Photoconductive antenna [28].

several milliwatts will most probably be created from a THz-QCL in the near future. It will also have relatively high power, compactness, smooth emission frequency tuning, and low power consumption.

Time-Domain THz-Spectroscopy and Active Spectral Imaging. Most THz-radiation applications can be divided into two groups, i.e., THz-spectroscopy itself and active THz-imaging [5, 7, 8, 12, 15]. Time-domain spectroscopic measurements (different scientific schools call it pulsed, variable, time-resolved spectroscopy, etc.) are made for pulsed THz-radiation. A principal feature of time-domain spectroscopy (TDS) is that the wave-field amplitude is measured directly as a function of time. This enables the characteristics of the examined substances to be obtained in the frequency range of the pulse spectrum [98–119]. Thus, the coherent nature of the generation and detection using a photoconductive antenna enables both the real and imaginary parts of the dielectric permittivity of an inspected object to be determined over a broad frequency range with a high signal-to-noise ratio. This method was called THz TDS or time-domain THz-spectroscopy in the foreign literature because the spectrum is obtained by recording the pulse wave shape [5, 7, 20].

Time-domain THz-spectroscopy. This method is based on the generation and detection of coherent THz-radiation using short femtosecond pulses (10–100 fs) from, as a rule, a single Ti:Sa laser. The laser radiation is divided into two beams, one of which excites ultra-short (1–10 ps) THz-pulses in a photoconductive antenna. The other is used to create a time strobe in the photodetector, the signal from which displays the electric-field profile of the THz-radiation (Fig. 12). Typical pulse lengths used in TDS are shown.

A photoconductive antenna is a plate of semiconductor (e.g., GaAs) onto which two parallel metal electrodes are placed, usually at a distance of 50–200 μm (Fig. 13). The antenna is used as a generator when a constant potential is applied to the metal electrodes. Charge carriers are generated in the semiconductor when a femtosecond laser pulse impinges on the plate. Also, a surface electric current $I(t)$ arises and generates an electromagnetic THz-pulse according to the Maxwell equation $E(t) \sim \partial I/\partial t$. Its spectrum is determined by the Fourier transform of its temporal shape (Fig. 14). Thus, the photo-semiconductor surface can be viewed as a dynamic antenna emitting pulses of broad-band electromagnetic radiation hundreds of femtoseconds in length. The semiconducting antenna parameters enable broad-band THz-pulses with a central frequency

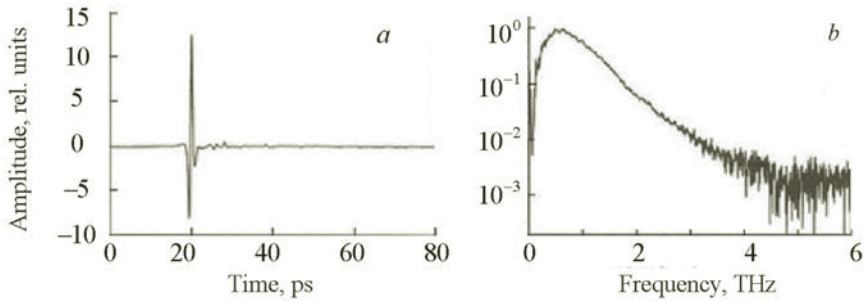

Fig. 14. Typical temporal shape of THz-pulse (photoconductive antenna of GaAs) (a); THz-pulse spectrum obtained using the Fourier transformation of its temporal shape (b) [120].

of 1–2 THz to be obtained [5, 98]. Semiconducting crystals of GaAs (LT-GaAs) [7, 116–125], InAs [117, 118, 126, 127], and InP [54, 117, 118, 122] are used most often as semiconducting antennae for generating THz-radiation.

The antenna is used as a THz-radiation detector if there is no potential between the electrodes. For this, charges formed in the semiconductor by the probe laser pulse migrate through the action of the THz-pulse field incident on the antenna with a time delay relative to the laser pulse. In this instance, the measured current passing between the electrodes is proportional to the THz-pulse electric field strength. If the time delay between pulses is varied, then the THz-pulse field strength as a function of time can be measured. Such detection is time-domain THz-spectroscopy. It allows not only the amplitude of the radiation passing through or reflected from the sample to be detected but also its phase. Thus, time-domain THz-spectroscopy, in contrast with traditional methods, enables all optical characteristics of an object (real and imaginary parts of the complex refractive index) to be determined from a single measurement without invoking the Kramers–Kronig equation.

Active spectral THz-imaging. THz-radiation lies in the mid-IR range [2] and can be used for active spectral imaging of an inspected object (THz-imaging). THz-imaging is a promising technology for standoff detection and identification of chemicals [8, 27]. The general concept developed before [20, 128–130] for pulsed spectral imaging based on pulsed THz-spectroscopy is rather simple.

Broad-band THz-radiation is focused on the studied target region. Characteristic absorption bands of the studied materials fall in the range of the THz-radiation. In turn, the target response to the action is recorded as diffusely scattered radiation using a detector, the field of view of which scans the irradiated region, e.g., using a system of mirrors. The object image formed with pulsed irradiation by broad-band THz-radiation has significant features compared with the analogous process, e.g., in the mid-IR range. This is due to the fact that each image point (pixel) from pulsed THz-irradiation contains information about the complete temporal shape of the pulses, i.e., about their amplitude and phase at any time point. In essence, this means that three coordinates, two spatial and one temporal, must be scanned in order to form the object image in the THz-range. Therefore, on one hand, pulsed imaging is much more informative than CW but, on the other, it takes longer to perform (about several minutes). Therefore, it is not applicable for real-time investigations. However, the measurement procedure is greatly simplified for the detection of objects for which knowledge of the spectrum is not required (e.g., cold or fire arms hidden under clothing). In this instance, reflected THz-radiation can be recorded using a broad-band source with a fixed time delay, e.g., at the wave front peak. This increases significantly the inspection throughput [5, 7, 8].

THz-QCL of sufficient power with a narrow emission line that operate in CW generation mode can be used for continuous imaging. A single THz-source is adequate for obtaining a monochromatic image, e.g., for forming an image of a strongly reflecting object (metal). If the studied object has features in the absorption spectrum, then the selectivity of the continuous imaging can be significantly increased by using several THz-QCL with frequencies falling in the characteristic absorption bands of the material. The procedure for forming a multi-spectral image is analogous to that examined for the mid-IR range [2].

Detection of Explosives Using THz-TDS and Active Imaging. As noted above, explosives are detected remotely in practice using two methods. These are remote detection where an operator controls remotely an inspection system installed on a mobile robotic platform and standoff detection where an operator and the inspection system are located at a safe distance from the inspected object.

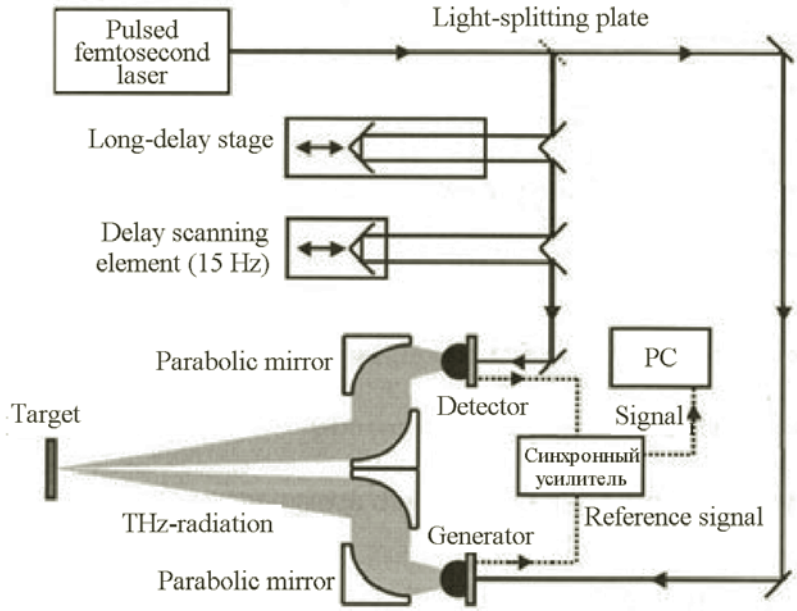

Fig. 15. THz-system with photoconductive dynamic antenna for standoff detection [20].

As a rule, the standoff detection system is more preferred because in this instance the possibility of losing expensive equipment is avoided. The fabrication of full-value standoff detection systems is a complicated problem that has not yet been solved. A number of serious unresolved issues apply to the THz-range as compared with the mid-IR range. First is the greater attenuation of the radiation in the atmosphere, a typical value of which is 50 dB·km^{-1} at 0.8 THz (this parameter only increases at higher frequencies) under normal conditions [5], and losses of radiation upon passage through masking material. Second is a problem related to the creation of powerful, compact, and room-temperature tuned THz-radiation sources. Third is the development of sensitive receivers and detection schemes. Finally, issues on the improvement of recognition algorithms of chemicals in multi-component media and the development of image processing methods remain unresolved.

Despite these problems, more and more studies focused on the application of THz TDS and active imaging to standoff detection of explosives are appearing [20, 131–141]. In the latter instance, not only spectral information about the studied substance but also its spatial relationship to the object can be obtained. For this, explosives are detected by creating an image at a frequency corresponding to its spectral feature. Thus, even explosive mixtures were identified according to their chemical and spatial distributions and the quantitative contents of the individual components in the target [140]. However, it is obvious that the probability of identification increases considerably if a source with a tunable emission frequency or a source with several emission lines that fall in the absorption band characteristic of the studied substance is available [1, 2].

The present review is limited to those studies in which various approaches to solving the issues that in our opinion are most promising for practical implementation are developed. Furthermore, as far as we know, these studies were the first (or one of the first) for each of the approaches and are currently the most developed for creating compact THz devices for standoff detection.

Detection using THz TDS. The possibility of using THz TDS for remote detection and identification of explosives in real-time mode under normal climatic conditions was examined [20]. Figure 15 shows a diagram of the used THz standoff system. It can be seen that it was a measuring system with a photoconducting dynamic antenna and a homodyne detection signal. The laser radiation source was a Ti:Sa laser with λ_{gen} = 800 nm, average radiation power 800 mW, pulse length 80 fs, and repetition rate 80 MHz. The laser beam was split into two parts using a light-splitting plate. One of them was the pump beam (20%) that acted on the photoconductive antenna that generated the THz-radiation; the other, a probe beam (80%) that detected the THz-radiation reflected from the object. The probe-beam channel contained a line with a constant delay of 1000 mm and one with a 15-Hz variable delay that formed the time strobe (both lines contained angle mirror reflectors). Hyperhemispherical lenses of high-ohmic Si were situated on the photoconductor surfaces in order to increase the THz-radiation collection efficiency [20, 141]. Two off-axis parabolic lenses with diaphragm number $f/1$ and gold-coated operating surfaces were used in the measurement system in order to collimate and focus the THz-radiation.

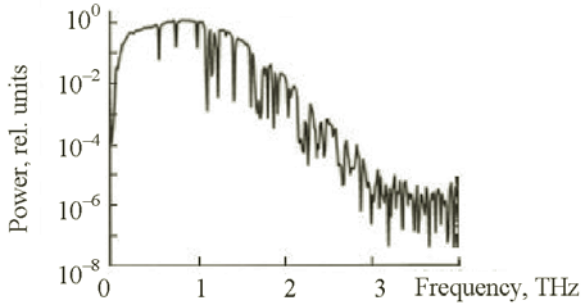

Fig. 16. Spectral dependence of power of THz-radiation reflected from a mirror; total path traversed by THz-radiation in atmosphere, 2.4 m [20].

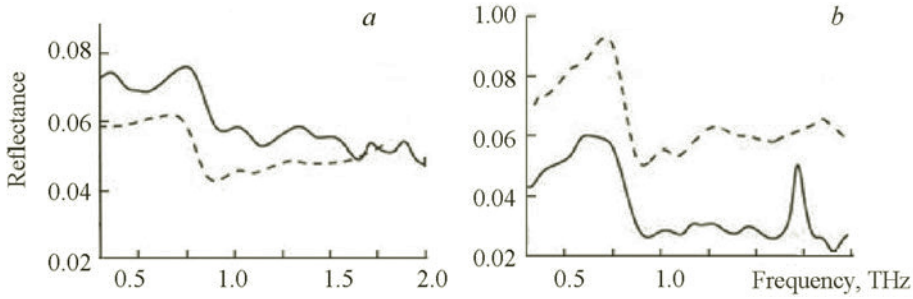

Fig. 17. Measured (solid line) and calculated (dashed line) reflectance spectra obtained at a distance of 1 m from two different explosives samples: Semtex-H (a) and SX2 (b) [20].

A mirror reflecting the THz-radiation was placed at the focus of the measurement system in order to demonstrate the fast-acting system and determine the dynamic range and frequency spectrum generated by the dynamic photoconducting antenna. Figure 16 shows the spectral dependence of the THz-radiation power reflected from the mirror. It can be seen that the measurement system dynamic range at a distance of 1 m from the object was >60 dB. The spectral band of the generated THz-pulse was in the range 0.1–3.0 THz. The time during which the THz-radiation spectrum was formed in the fast-acting systems was 1/15 s (system time constant). The sharp features of the spectrum that were related to absorption of THz-radiation by the atmosphere at a distance of 2.4 m (optical path length) were interesting. These could be removed by using a special algorithm. It can be seen that rather narrow and numerous transmission windows through which a signal could pass practically without attenuation were present in the water-vapor absorption band.

Figure 17 shows standoff reflectance spectra from two different explosives samples (Semtex-H and SX2) that were obtained at a distance of 1 m during 1/15 s. The absolute values of the reflectance from the samples were found by normalizing the measured function to previously obtained values of reflectance from the mirror. Good agreement with the calculated values can be seen. In both instances, spectral features at 0.8, 1.05, and 1.4 THz (the frequencies are the same because both samples contained RDX as the main component) appeared. The data were processed in 1/15 s and used an algorithm that removed the effect of water vapor.

Clothing plays a decisive role in concealing explosives or fire arms. Therefore, masking of explosives using it was studied. The studies consisted of finding the minimum number of clothing layers under which the presence of explosives could not be determined. The clothing layers were ordinary shirts fabricated from typical cotton/polyester blends. Figure 18 illustrates the masking effect associated with the number of clothing layers. It can be seen that the reflectance decreased rapidly with increasing radiation frequency. This was a direct consequence of the exponential increase of absorption with increasing number of clothing layers (cloth thickness). The clothing suppressed the high-frequency portion of the spectrum, i.e., acted as a filter for low frequencies. The observed pattern could be corrected by taking the derivative of the normalized reflected radiation power over frequency, in other words, by examining the differential reflectance spectrum, which is shown in Fig. 18b. In this instance, the spectral features of SX2 are clearly visible at all characteristic frequencies up to four clothing layers. However, the spectral features of the explosives are difficult to identify even through two clothing layers using the ordinary spectrum (Fig. 18a).

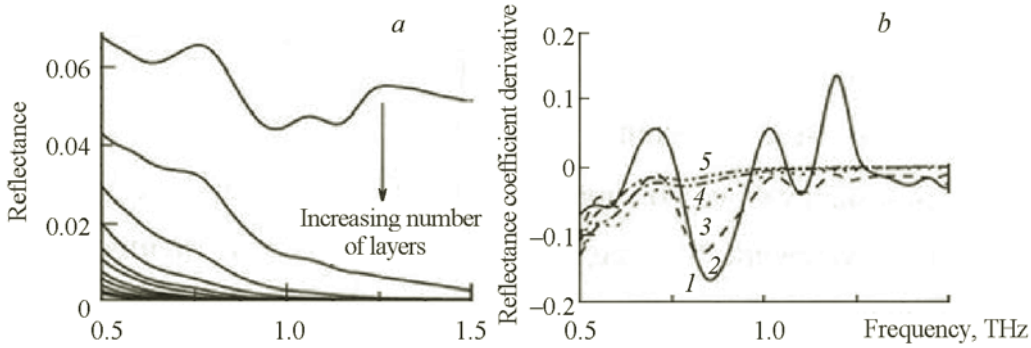

Fig. 18. Measured frequency dependence of THz-radiation reflectance from SX2 hidden under cotton clothing (a) and its first derivative (b); number of clothing layers: 0 (1), 1 (2), 2 (3), 3 (4), and 4 (5) [20].

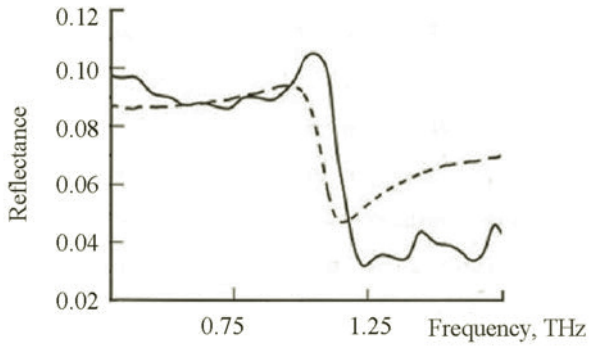

Fig. 19. Measured (solid curve) and calculated (dashed curve) reflectance spectra of *d*-tartaric acid at a standoff distance of 1 m [20].

As noted several times, the most common types of explosives have characteristic spectral features in the THz-range. Also, relatively few hazardless materials have their own characteristic fingerprints in this spectral range. As an example, let us examine *d*-tartaric acid, which has characteristic features in the examined frequency range (Fig. 19). Measurements were made at a distance of 1 m under normal atmospheric conditions. The reflectance measurements over the whole spectral range were processed using a fast-acting algorithm that removed the effect of water. Data obtained by transmission spectroscopy were used to compare the calculated reflectance spectra of *d*-tartaric acid with the experimental results. It was interesting to compare Figs. 19 and 6. It can be seen that the calculations agreed well with the experimental results. Although the shape of the *d*-tartaric acid reflectance spectrum was similar to that of RDX, the central frequency and the magnitude of the reflectance were different, which demonstrated that their spectral difference could be used, i.e., the method enabled explosives to be identified in the presence of interferences. The effect of possible interferences on the detection of RDX, PETN, HMX, TNT, SX2, and Semtex-H was discussed before [142]. Those results confirmed that materials encountered on a daily basis did not exhibit pronounced spectral features in the THz-range where they appeared in the studied explosives and; therefore, did not prevent explosives from being detected.

Reflectance spectra of RDX situated under masking layers of various materials (paper, polyethylene, leather, polyester) were measured at a distance of 0.5 m [143]. Problems associated with recording signals at frequencies >1 THz arose because of absorption by water vapor. The RDX peak at 0.82 THz appeared rather clearly despite the presence of masking materials that distorted the reflectance spectrum.

The distance of standoff detection of explosives was studied [144]. The researchers observed at a distance of 30 m and a THz TDS frequency of 0.82 THz a slightly broadened but clearly distinguishable peak characteristic of the RDX absorption spectrum. Despite the successful use of pulsed laser generation to obtain broad-band THz-radiation, several factors limited the potential of this direction [7], among which the main one was the rather low energy transformation efficiency of the optical pulse into THz-wave energy (~0.1%) [7, 103].

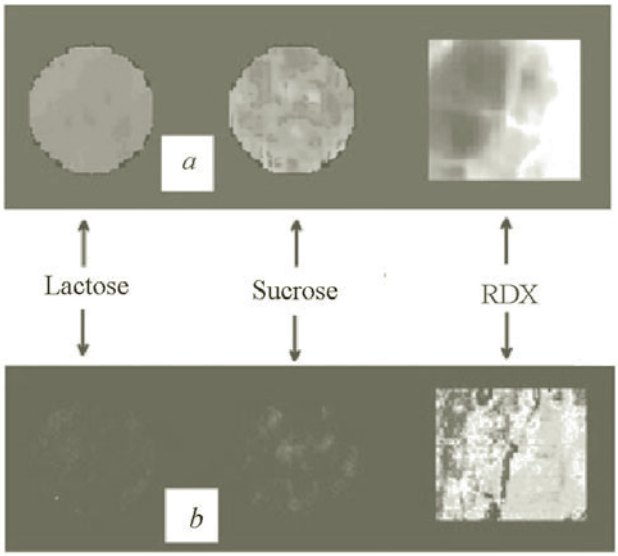

Fig. 20. THz-image in artificial light tones of spatially separated chemical compounds: lactose, sucrose, and RDX (a); RDX detection after applying an image processing algorithm (PCA) and comparing with library absorption spectra of known materials (b) [130].

Detection using active imaging systems based on THz QCL. The combination of image-formation and THz-spectroscopy methods is an effective means for inspecting objects for hidden explosives and cold arms. THz TDS was used for personal inspection [141]. The detected object was a small item in the form of sticks of the plastic explosive SX2 attached to the human body and hidden beneath several layers of leather clothing. The explosive was observed as a non-uniformity on the skin of the test subject that was due to differences in the reflectance of human skin and the object surface. The explosive was not identified in the study. Thus, the need to develop procedures and algorithms for solving this problem was noted.

The ability to detect and distinguish explosives from interferences during imaging in the THz-range was first demonstrated by Shen et al. [145], where the reflectance spectrum of THz-radiation from granules of lactose, sucrose, and RDX was studied (Fig. 20a). Significant contrast was observed between images of objects that was related to differences in absorption spectra of the studied substances in this range. The absorption spectrum of each image pixel was analyzed using principal component analysis (PCA) in order to identify the substances. Then, they were compared with available library spectra. Figure 20b shows a portion of the image processing that enabled the identification of RDX particles (bright pixels) to be demonstrated.

Another example of a THz-imaging system was examined theoretically [24]. THz-imaging (0.3–10 THz) is known to be based on the existence in this frequency range of characteristic features in absorption spectra of explosives. Radiation sources of rather high power are needed in order to perform it in real time. Furthermore, THz-imaging systems should be located at distances of 10–25 m from the inspected object in order to ensure safe working conditions. This requirement limits the choice of available THz frequencies to narrow bands of atmospheric transparency. These bands (Fig. 3) occupy an interval of several hundred gigahertz, outside of which absorption by water vapor that, as a rule, exceeds 10 dB/m has an effect. Increasing the THz-radiation power led only to a logarithmic increase of the detection distance because of the exponential growth of absorption losses. Therefore, the choice of THz-radiation frequency within these windows is of fundamental significance for standoff applications. This factor makes THz QCL the most suitable radiation source because it has a very narrow generation line and high emission power (~500 mW in pulsed mode and ~130 mW in CW mode) [27, 146]. Furthermore, the operating principle of QCL based on intra-band transitions presupposes that any frequencies in the range 1–5 THz can be produced for the appropriate engineering designs (Table 1). The last condition should be expected to enable the operation of THz-radiation sources to be optimized by taking into account atmospheric transmission bands and the spectral features of the examined explosives. Three basic types of THz-imaging systems, the parameters of which are compared in Table 2, were examined as possible versions [24, 147].

Table 2. Possible Versions of THz Imaging Systems and Their Principal Characteristics

THz-imaging system	Principal characteristics
Single-element detector; scanning mirror; heterodyne detection	High sensitivity; slow response rate; complicated set up
Single-element detector, scanning mirror; without heterodyne detection	Relatively low sensitivity; slow response rate; simple set up
Matrix (FPA) detector; one laser irradiating the whole studied region	Relatively low sensitivity, rapid response rate; simple set up

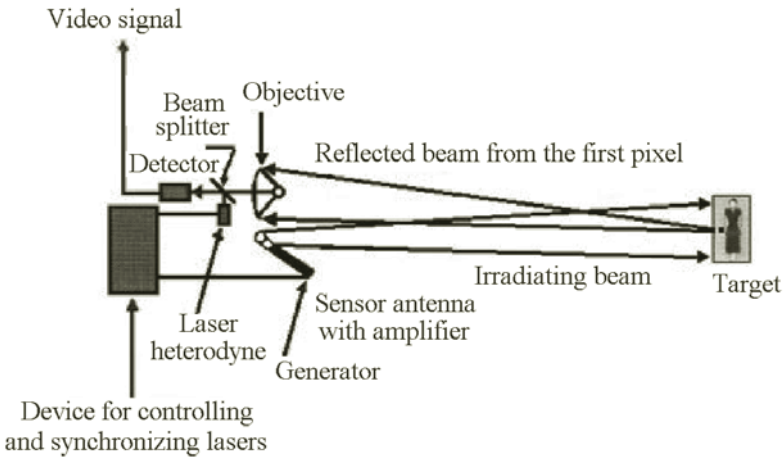

Fig. 21. Diagram of system for imaging standoff detection of explosives in the terahertz range using quantum-cascade lasers and heterodyne detection [24].

The system sensitivity in combination with the principal elements used in it that operate at room temperature are important for a standoff imaging system. Of the three possible versions shown in Table 2, the researchers chose the first, i.e., with heterodyne detection, by considering that room-temperature THz QCL will emerge and room-temperature detectors based on Schottky diodes will be available [24]. It is noteworthy that Schottky diodes, which have a broad transformation band and can operate over a broad temperature range, require ~1 mW of heterodyne power. Such a power level is difficult to produce in compact solid-state sources currently available except for THz QCL. Heterodyne detection using THz QCL was first demonstrated experimentally in 2005 [60]. However, the researchers did not consider the rapid response time of the system that is important for remote inspection in selecting a promising imaging system. In this respect, the third version given in Table 2 had indisputable advantages. Perhaps for this reason, the researchers considered the third version that enabled operation in real time to be promising [147–150].

Let us analyze briefly the first of these studies [24]. The most optimistic data for remote detection, to which we will refer later, should be obtained in this study by taking into account the highest sensitivity of the examined system and the choice of radiation-source frequency falling in the atmosphere transmission window. A portable imaging system including two independent THz QCL, the principal parameters of which were studied theoretically taking into account quenching of the THz-radiation in the atmosphere, the sizes of the emitting and receiving antennae, the laser power, and the radiation detector sensitivity, was proposed in it. The atmosphere window in the range 1.5 THz that is today most promising for measurements using a QCL was examined. The parameters of imaging standoff systems based on ultrasensitive heterodyne detection were analyzed in detail. A THz QCL was used as the pump laser and the probe laser. Calculations were performed for laser emission power 10 mW. However, as noted above, such lasers may have in the future a power level of ~100 mW for the proposed system (Fig. 21).

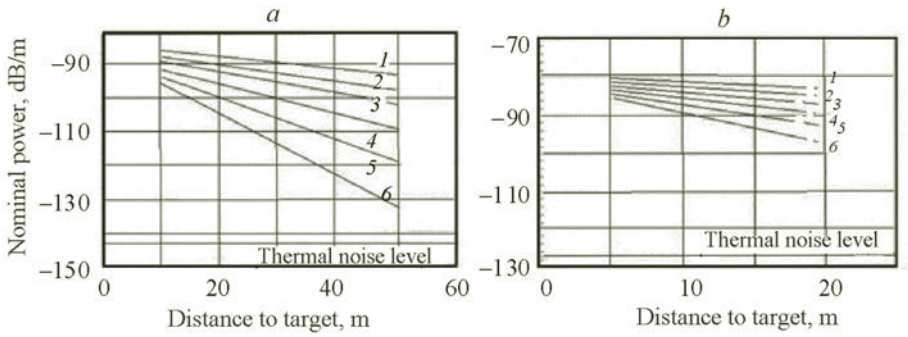

Fig. 22. Power as a function of distance from target obtained for standoff imaging system at relative humidity (RH) = 10 (1), 20 (2), 30 (3), 40 (4), 50 (5), and 60% (6): resolution 10 × 10 cm and video channel transmission band 1 kHz (a); resolution 1 × 1 cm, predicted system characteristics exceed by 37 dB the noise level in the 50-kHz band (b) [24].

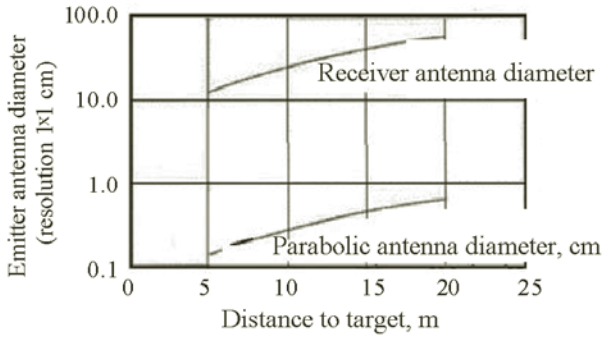

Fig. 23. Optimal antenna sizes for receiver and emitter as functions of distance to target [24].

A portable standoff system with a heterodyne detector that uses a THz QCL seems to be the most sensitive of known systems for standoff detection of weapons and explosives hidden under clothing. However, as shown before [24], even this system that is calculated for an emission frequency of 1.5 THz and has spatial resolution of 1 × 1 cm (pixel size on the target) at a distance of 50 m does not provide sufficient sensitivity at normal humidity.

Two versions combined for improved sensitivity were examined realistically for elevated humidities, i.e., by decreasing the resolution or distance. Thus, decreasing the image resolution from 1×1 cm to 10 × 10 cm provided acceptable sensitivity at target distances up to 50 m whereas retaining a pixel size of 1 × 1 cm enabled sufficient sensitivity to be attained at a distance of ~10 m (Fig. 22). Intermediate combinations of resolution/distance could also provide the required system sensitivity. However, higher resolution than 1 × 1 cm were required to detect hidden weapons.

Figure 22 shows that a buffer of ~10 dB existed for reliable signal recording at 60% humidity at a distance to the target of 10 m, receiver noise of ~10 dB, and clothing losses of ~20 dB. Figure 23 shows the optimum antenna sizes for the receiver and emitter as functions of the distance to the target in the examined scenario. The results provided an idea of the dimensions of the THz-imaging system with heterodyne detection together with the sensitivity (detection distance). This was important for determining possible applications of it.

An alternative device configuration for THz-imaging standoff detection of explosives using a QCL and matrix focal-plane array (FPA) receiver for producing an image over a broad field of view and in real time was described [148]. The researchers developed subsequently this idea by attempting to create a full-value standoff device for THz-imaging based on a THz QCL and an FPA receiver [148–151].

The ability to produce an image of an object that was opaque in visible light (maple leaf seed) and was situated at a distance of ~25 m from the radiation source using a system in which THz-radiation passing through the object was recorded was demonstrated [147].

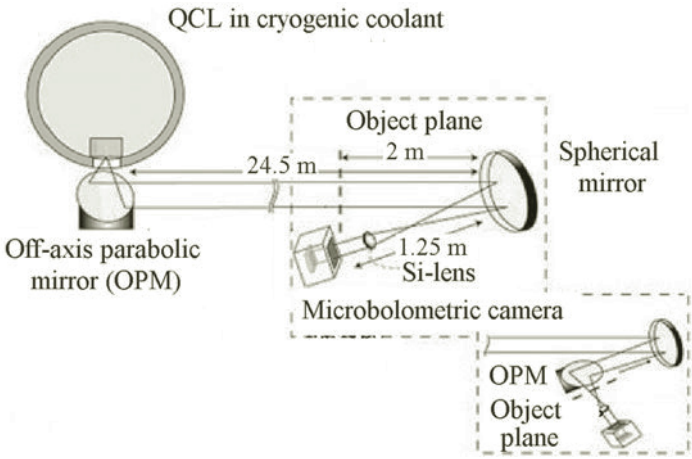

Fig. 24. Diagram of experimental set up for imaging an object by recording THz-radiation from a QCL that passes through it [148].

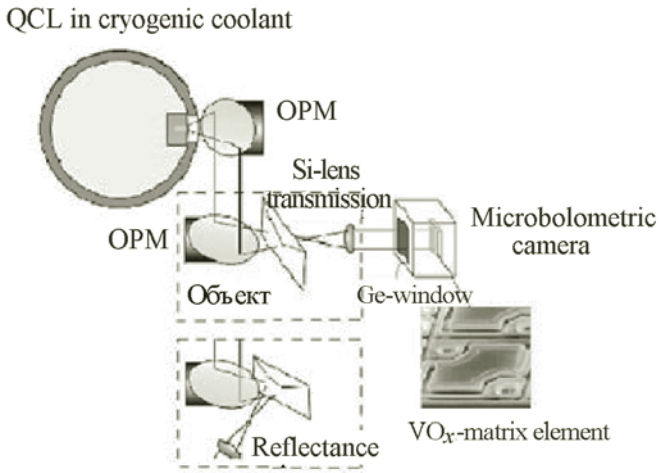

Fig. 25. Diagram of experimental QCL THz-imaging system and vanadium oxide microbolometric matrix operating in real-time mode; time for image production including signal processing is 1/20 s [149].

Thus, a critical parameter for such distances was the THz QCL wavelength. Therefore, a QCL emitting at ~4.9 THz, which falls in one of the windows of atmospheric transmission with comparatively low losses (0.51 dB/m), was developed. Without going into the QCL design details [148], we note only that the population inversion in the active medium arose because the lower working level was depleted as a result of resonant emission of an optical phonon. The peak laser emission power was 17.5 mW with pulse length 13.5 ms and population coefficient (a quantity inverse to the pulse length) 27%. The QCL operating temperature of 30 K was maintained by placing it in a cryostatic cooler (closed-cycle cryogenic refrigerator using pulse tubes). The image was recorded using a room-temperature bolometric camera (320 × 240, NEP ~ $3.2 \cdot 10^{-10}$ $W \cdot Hz^{-1/2}$ at 4.3 THz) and subtracting the constant background. Figure 24 shows various configurations of the experimental set up for recording the object. The signal-to-noise ratio measured at a distance of 25 m was 2.5 for one frame and 10 for averaging over 20 frames (recording rate 20 frames/s).

One of the most important imaging parameters, the image formation time, was addressed before [149–152]. The overwhelming majority of THz images until now were obtained by scanning the object using a focused beam of THz-radiation (TDS pulsed imaging). Naturally, the information collection time was highly limited by the mechanical scanning rate. The whole object image could be obtained in several minutes if the mechanical scanning rate upper limit was taken as ~100 pixels/s.

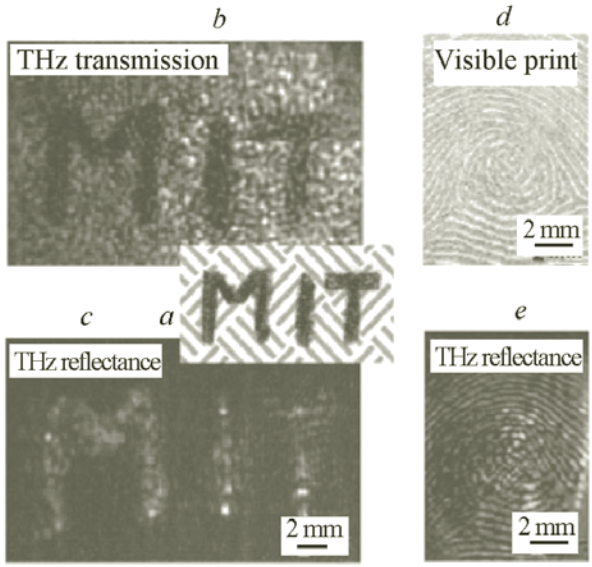

Fig. 26. Script written in pencil on the inside of a security envelope: in the visible spectral range (a); in the THz-range obtained for transmission in one frame (1/20 s) (b); in the THz-range obtained for reflection by averaging 20 frames over 1 s (c); visible thumb print (d); image of thumb print obtained in THz-range using reflectance averaged over 1 s (20 frames) (e) [149].

The unique properties of THz QCL radiation in combination with matrix FPA-receivers can be used to obtain object images in real time [150]. THz-imaging using a CW THz QCL and a room-temperature matrix bolometric radiation receiver was demonstrated for the first time in 2006 [149]. Figure 25 shows a diagram of the experimental set up. The THz QCL was cooled to ~30 K using a pulsed-tube closed cycle cryogenic refrigerator. The radiation power was ~50 mW. The studies used both transmission and reflectance modes. A differential scheme for subtracting the background radiation from the recorded signal and decreasing the flicker noise ($1/f$) was developed. Figure 26 shows images obtained in real time (1/20 s). Images in the THz-range of several written symbols within a security envelope that were obtained in transmission and reflectance modes are clearly visible. These images could not be obtained in other spectral ranges. X-rays did not provide the required contrast. Millimeter waves did not give adequate spatial resolution. IR radiation was strongly scattered and/or absorbed in the material fibers.

The availability of a coherent tuned source with a narrow generation band plays a decisive role in applications involving the detection and identification of explosives where narrow spectral lines characteristic of the studied substance must be recorded. The examined system with additional THz QCL can produce multi-spectral images of objects in real time. The emergence of THz QCL tuned over a broad spectral range enables colored spectral images to be formed. This increases considerably the information about the object and increases the probability that it will be identified.

It can now be considered established that THz-imaging has great potential and high efficiency for detecting and identifying hidden explosive devices and cold and fire arms. However, issues with the background spectral noise, the effect of material concealment (presence in them of multiple reflections and strong absorption), similarity of spectra in the THz-range, effect of atmospheric humidity, etc. remain unresolved. Much research, including the development of calculation methods, must be performed in order to resolve them.

Conclusions. The unique property of THz-radiation related to its penetration through clothing, paper, wood, plastics, ceramics, and other materials presents broad possibilities for applying the technology to THz spectroscopy to provide security, especially for exposing terrorists in large crowds. A decisive factor is the harmless interaction of this radiation with biological objects.

THz QCL are currently the brightest solid-state sources of CW radiation that operate above liquid N_2 temperature. A literature review left no doubt that the appearance of tuned THz QCL that operate at room temperature should be expected in the near future. One promising approach for solving the problem is DFG. However, as already noted, construction designs

and active materials different in principle from existing ones must be used for this. This has already been confirmed. Thus, the use of non-traditional designs led to the creation of THz QCL with unique parameters compared with all other type of solid-state THz sources. The laser operates in CW mode at room temperature with emission power in one mode of 0.2 mW. The researchers suggested that the operating range will span 1–4.6 THz in the near future.

It seems justified to propose that standoff devices for detecting explosives will in the future be combined systems based on the use of orthogonal technologies. Modern technologies enable THz spectroscopy to be combined with IR spectroscopy in a single portable device. This expands considerably the applications and gives the device new functional capabilities. Such systems may play the decisive role in standoff applications.

An analysis of the research results showed only the possibility in principle for THz-imaging of hidden explosives and cold and fire arms. Much research should still be performed in order to improve the detection technology and to develop methods for analyzing the spectral data and processing the images. The main problem to be solved before the THz technology for detecting hidden explosives can be deployed in the field is related to the creation of a compact tunable room-temperature THz emitter of sufficient power.

REFERENCES

1. L. A. Skvortsov and E. M. Maksimov, *Kvantovaya Elektron. (Moscow)*, **40**, 565–575 (2010).
2. L. A. Skvortsov, *Kvantovaya Elektron. (Moscow)*, **41**, 1051–1060 (2011).
3. L. A. Skvortsov, *Kvantovaya Elektron. (Moscow)*, **42**, 1–11 (2012).
4. V. Karasik, V. Ryzhii, I. Fokina, and L. Chlenova, *Vestn. Mosk. Gos. Tekh. Univ. im. N. E. Baumana. Priborostroenie, Spets. Vyp.*, No. 9, 5–19 (2012).
5. M. Kemp, *Proc. SPIE Int. Soc. Opt. Eng.*, **6402**, 64020D-1–19 (2006).
6. V. G. Bespalov, in: *Problems in Coherent and Non-linear Optics* [in Russian], I. P. Gurov and S. A. Kozlov (Eds.), SPBGU ITMO, St. Petersburg (2006), pp. 63–66.
7. B. Liu, H. Zhong, N. Karpovicz, Y. Chen, and X.-C. Zhang, *Proc. IEEE*, **95**, 1514–1527 (2007).
8. *Terahertz (THz) Imaging.* AFRL-SN-RS-TR-2006-69, In-House Interim Report, Rome, New York (2006).
9. V. L. Bratman, A. G. Litvak, and E. V. Suvorov, *Usp. Fiz. Nauk*, **181**, 867–874 (2011).
10. B. N. Zvonkov, A. A. Biryukov, S. M. Nekorkin, V. Ya. Aleshkin, V. I. Gavrilenko, A. A. Dubinov, K. V. Marem′yanov, and S. V. Morozov, *Fiz. Tekh. Poluprovodn.*, **43**, No. 2, 220–223 (2009).
11. A. Davies, A. Burnett, W. Fan, E. Linfield, and J. Cunningham, *Mater. Today*, **11**, 18–26 (2008).
12. S. L. Dexheimer (ed.), *Terahertz Spectroscopy: Principles and Applications*, CRC Press, Taylor and Francis Group, (2008).
13. M. Nazarov and A. Shkurinov, *Izv. Vyssh. Uchebn. Zaved., Radiofiz.*, **52**, No. 7, 576–582 (2009).
14. K. B. Mikitchuk and A. A. Afonenko, *Fiz. Tekh. Poluprovodn.*, **46**, No. 1, 121–124 (2012).
15. M. Tonouchi, *Nat. Photonics*, **1**, 97–105 (2007).
16. Z. Bielecki, J. Janucki, A. Kawalec, J. Mikolajczyk, N. Palka, M. Pasternak, T. Pustelny, T. Stacewicz, and J. Wojtas, *Metrol. Meas. Syst.*, **XIX**, 3–28 (2012).
17. C. Schmuttenmaer, *Chem. Rev.*, **104**, 1759–1779 (2004).
18. http://www.ispoptics.com/admuploads/file/highresistivitysioverview.pdf.
19. X.-C. Zhang and J. Xu, *Introduction to THz Wave Photonics*, Springer-Science + Business Media, LLC (2010).
20. T. Kubis, C. Yeh, P. Vogl, A. Benz, G. Fasching, and C. Deutsch, *Phys. Rev. B: Condens. Matter Mater. Phys.*, **79**, 195323-10 (2009).
21. A. Tuchak, G. Gol′tsman, G. Kitaeva, A. Penin, S. Seliverstov, M. Finkel′, A. Shepelev, and P. Yakunin, *Pis'ma Zh. Eksp. Teor. Fiz.*, **96**, 97–101 (2012).
22. M. Walther, B. Fischer, A. Ortner, A. Bitzer, A. Thoman, and H. Helm, *Anal. Bioanal. Chem.*, **397**, 1009–1017 (2010).
23. B. N. Behnken, G. Karunasiri, D. R. Chamberlin, P. R. Robrish, and J. Faist, *Opt. Lett.*, **33**, 440–442 (2008).
24. K. Linden and W. Neal, in: *Proc. 34th Appl. Imagery Recognition Workshop*, IEEE Computer Society, Washington, D.C. (2005), pp. 7–14.
25. C. Walther, G. Scalari, J. Faist, H. Beere, and D. Ritchie, *Appl. Phys. Lett.*, **89**, 231121-3 (2006).
26. C. Walther, M. Fisher, G. Scalari, R. Terazzi, N. Hoyler, and J. Faist, *Appl. Phys. Lett.*, **91**, 131122-1 (2007).
27. B. Williams, *Nat. Photonics*, **1**, 517–525 (2007).
28. D. Allis, D. Prokhorova, and T. Korter, *J. Phys. Chem.*, **110**, 1951–1959 (2006).

29. D. Allis, J. Zeitler, P. Taday, and T. Korter, *Chem. Phys. Lett.*, **463**, 84–89 (2008).
30. B. Ferguson and X.-C. Zhang, *Nat. Mater.*, **1**, 26–33 (2002).
31. D. Allis and T. Korter, *Int. J. High Speed Electron. Syst.*, **17**, 193–212 (2007).
32. Q. Chow, C. Zhang, K. Mu, B. Jin, L. Zhang, W. Li, and R. Feng, *Appl. Phys.*, **92**, 101106-3 (2008).
33. M. Leahy-Hoppa, M. Fitch, and R. Osiander, *Anal. Bioanal. Chem.*, **395**, 247–257 (2009).
34. A. Burnett, W. Fan, P. Upadhya, J. Cunningham, H. Edwards, M. Hargreaves, E. Linfield, and G. Davies, *Proc. SPIE Int. Soc. Opt. Eng.*, **6402**, 64020B-7-12 (2006).
35. J. Melinger, N. Laman, and D. Grischkowsky, *Appl. Phys. Lett.*, **93**, 011102-3 (2008).
36. Y. Hu, P. Huang, L. Guoa, X. Wang, and C. Zhang, *Phys. Lett. A*, **359**, 728–732 (2006).
37. M. Kemp, P. Taday, B. Cole, J. Cluff, A. Fitzgerald, and W. Tribe, *Proc. SPIE Int. Soc. Opt. Eng.*, **5070**, 44–52 (2003).
38. Y. Chen, H. Liu, Y. Deng, D. Schauki, M. Fitch, R. Osiander, C. Dodson, J. Spicer, M. Shur, and X.-C. Zhang, *Chem. Phys. Lett.*, **400**, 357–361 (2004).
39. A. Shabaev, S. Lambrakos, N. Bernstein, V. Jacobs, and D. Finkenstadt, *Appl. Spectrosc.*, **65**, No. 4, 409–416 (2011).
40. J. Chen, Y. Chen, H. Zhao, G. Bastiaans, and X.-C. Zhang, *Opt. Express*, **15**, 12060–12067 (2007).
41. Y. Chen, H. Liu, M. Fitch, R. Osiander, J. Spicer, M. Shur, and X.-C. Zhang, *Proc. SPIE Int. Soc. Opt. Eng.*, **5799**, 19–24 (2005).
42. M. Fitch, M. Leahy-Hoppa, E. Ott, and R. Osiander, *Chem. Phys. Lett.*, **443**, 284–288 (2007).
43. Y. C. Shen, P. C. Upadhya, E. H. Linfield, H. E. Beer, and A. G. Davies, *Appl. Phys. Lett.*, **83**, 3117–3119 (2003).
44. D. Petkie, F. De Lucia, C. Casto, P. Helminger, E. Jacobs, S. Moyer, S. Murrill, C. Halford, S. Griffin, and C. Franck, *Proc. SPIE Int. Soc. Opt. Eng.*, **5989**, 598918-8 (2005).
45. A. Gatesman, A. Danylov, T. Goyette, J. Dickinson, R. Giles, W. Goodhue, W. Waldman, W. Nixon, and W. Hoen, *Proc. SPIE Int. Soc. Opt. Eng.*, **6212**, 62120E1-13 (2006).
46. H. Kazianka, R. Leitner, and J. Pilz, *Segmentation and Classification of Hyper-Spectral Skin Data*, University of Klagenfurt, Institute of Statistics, Klagenfurt, Austria, CTR Carinthian Tech. Research AG, 9524 Villach, Austria (2008), pp. 245–252.
47. T. Yuan, H. Liu, J. Xu, F. Al-Douseri, Y. Hu, and X. Zhang, *Proc. SPIE Int. Soc. Opt. Eng.*, **5070**, 28–37 (2003).
48. J. T. Kindt and C. A. Schmuttenmaer, *J. Phys. Chem.*, **100**, 10373–10379 (1996).
49. I. Morino, K. M. T. Yamada, and A. G. Maki, *J. Mol. Spectrosc.*, **196**, 131–138 (1999).
50. R. D. Averitt, G. Rodriguez, J. L. W. Siders, S. A. Trugman, and A. J. Taylor, *J. Opt. Soc. Am. B: Opt. Phys.*, **17**, 327–331 (2000).
51. Y. Ding and I. Zotova, *Opt. Quantum Electron.*, **32**, 531–552 (2000).
52. A. Rice, Y. Jin, X. F. Ma, X.-C. Zhang, et al., *Appl. Phys. Lett.*, **64**, 1324–1326 (1994).
53. A. Stepanov, L. Bonacina, S. Chekalin, and J.-P. Wolf, *Opt. Lett.*, **33**, No. 21, 2497–2499 (2008).
54. B. Greene, P. Saeta, R. Douglas, and S. Chuang, *IEEE J. Quantum Electron.*, **28**, 2302–2312 (1992).
55. A. Nahata, A. Weling, and T. Heinz, *Appl. Phys. Lett.*, **69**, 2321–2323 (1996).
56. T. Loffler, T. Hahn, M. Thomson, F. Jacob, and H. Roskos, *Opt. Express*, **13**, 5353–5362 (2005).
57. K. Liu, J. Xu, and X.-C. Zhang, *Appl. Phys. Lett.*, **85**, 863–865 (2004).
58. W. Shi, Y. Ding, N. Fernelius, and K. Vodopyanov, *Opt. Lett.*, **27**, 1454–1456 (2002).
59. J. Herbling, A. Stepanov, G. Almasi, B. Bartal, and J. Kuhl, *Appl. Phys. B: Lasers Opt.*, **78**, 593–597 (2006).
60. J. Gao, J. Hovenier, Z. Yang, J. Baselmans, A. Baryshev, M. Hajenius, T. Klapwijk, A. Adam, T. Klaassen, B. Williams, S. Kumar, and Q. Hu, *Appl. Phys. Lett.*, **86**, 244104-5 (2005).
61. S. Barbieri, J. Alton, C. Baker, T. Lo, H. Beere, and D. Ritchie, *Opt. Express*, **13**, 6497–6503 (2005).
62. B. S. Karasik and R. Cantor, *Appl. Phys. Lett.*, **98**, 193503-3 (2011).
63. M. Rochat, L. Ajili, H. Willenberg, J. Faist, H. Beere, G. Davies, E. Linfield, and D. Ritchie, *Appl. Phys. Lett.*, **81**, 1381–1383 (2002).
64. R. Kohler, A. Tredicucci, F. Beltram, H. E. Beere, E. H. Linfield, A. G. Davies, D. A. Ritchie, R. C. Iotti, and F. Rossi, *Nature*, **417**, 156–159 (2002).
65. B. Williams, S. Kumar, Q. Hu, and J. Reno, *Opt. Express*, **13**, 3331–3339 (2005).
66. L. Li, L. Chen, J. Zhu, J. Freeman, P. Dean, A. Valavanis, A. G. Davies, and E. Linfield, *Electron. Lett.*, **50**, 309–311 (2014).
67. M. Belkin, Q. Wang, C. Pflugl, A. Belyanin, S. Khanna, A. Davies, E. Linfield, and F. Capasso, *IEEE J. Sel. Top. Quantum Electron.*, **15**, 952–967 (2009).
68. K. Vijayraghavan, Y. Jiang, M. Jang, A. Jiang, K. Choutaquanta, A. Vizbaras, F. Demmerle, G. Boehm, M. C. Amann, and M. A. Belkin, *Nat. Commun.*, **4**, 1–7 (2013).
69. O. Y. Lu, N. Bandyopadhyay, S. Slivken, Y. Bai, and M. Razeghi, *Opt. Express*, **21**, No. 1, 968–973 (2013).

70. O. Y. Lu, N. Bandyopadhyay, S. Slivken, Y. Bai, and M. Razeghi, *Appl. Phys. Lett.*, **101**, No. 25, 251121-3 (2012).
71. K. Vijayraghavan, R. W. Adams, A. Vizbaras, M. Jang, C. Grasse, G. Boehm, M. C. Amann, and M. A. Belkin, *Appl. Phys. Lett.*, **100**, No. 25, 251104-4 (2012).
72. Q. Y. Lu, N. Bandyopadhyay, S. Slivken, Y. Bai, and M. Razeghi, *Appl. Phys. Lett.*, **103**, 011101-3 (2013).
73. E. Dupont, S. Fathololoumi, Z. R. Wasilewski, G. Aers, S. R. Laframboise, M. Lindskog, S. G. Razavipour, A. Wacker, D. Ban, and H. C. Liu, *J. Appl. Phys.*, **111**, No. 7, 073111-1–10 (2012).
74. P. Dean, Y. L. Lim, A. Valavanis, R. Kliese, M. Nikolic, S. P. Khanna, M. Lachab, D. Indjin, Z. Ikonic, P. Harrison, A. D. Rakic, E. H. Linfield, and A. G. Davies, *Opt. Lett.*, **36**, No. 13, 2587–2589 (2011).
75. B. Williams, S. Kumar, Q. Hu, and J. Reno, *Electron. Lett.*, **42**, 89–90 (2006).
76. H.-W. Hubers, S. Pavlov, A. Semenov, R. Kohler, L. Mahler, A. Tredicucci, H. Beere, D. Ritchie, and E. Linfield, *Opt. Express*, **13**, 5890–5896 (2005).
77. S. Kumar, Q. Hu, and J. Reno, *Appl. Phys. Lett.*, **94**, 131105-3 (2009).
78. A. Lee and Q. Hu, *Opt. Lett.*, **30**, 2563–2565 (2005).
79. M. Belkin, J. Fan, S. Hormoz, F. Capasso, S. Khanna, M. Lachab, A. Davies, and E. Linfield, *Opt. Express*, **16**, 3242–3248 (2008).
80. M. Belkin, F. Capasso, F. Belyanin, M. Fischer, A. Wittmann, and J. Faist, *Appl. Phys. Lett.*, **92**, 201101-2 (2008).
81. M. Amanti, M. Fischer, G. Scalari, M. Beck, and J. Faist, *Nat. Photonics*, **3**, 586–590 (2009).
82. S. Kumar, C. Chan, Q. Hu, and J. Reno, *Nat. Phys.*, **7**, 166–171 (2011).
83. S. Fathololoumi, E. Dupont, C. Chan, Z. Wasilewski, S. Laframboise, D. Ban, A. Matyas, C. Jirauschek, Q. Hu, and H. Liu, *Opt. Express*, **20**, 3866–3876 (2012).
84. H. Richter, M. Greiner-Bar, S. Pavlov, A. Semenov, M. Wienold, L. Schrottke, M. Giehler, R. Hey, H. Grahn, and H.-W. Hubers, *Opt. Express*, **18**, 10177–10187 (2010).
85. S. Barbieri, P. Gellie, G. Santarelli, L. Ding, W. Maineult, C. Sirtori, R. Colombelli, H. Beere, and D. Ritchie, *Nat. Photonics*, **4**, 636–640 (2010).
86. P. Khosropanah, A. Baryshev, W. Zhang, W. Jellema, J. Hovenier, J. Gao, T. Klapwijk, D. Paveliev, B. Williams, S. Kumar, Q. Hu, J. Reno, B. Klein, and J. Hesler, *Opt. Lett.*, **34**, 2958–2960 (2009).
87. S. Kumar, *IEEE J. Sel. Top. Quantum Electron.*, **17**, 38–47 (2011).
88. A. Semenov, L. Mahler, A. Tredicucci, H. Beere, D. Ritchie, and H.-W. Hubers, *Appl. Phys. Lett.*, **96**, 071112-3 (2010).
89. S. Kumar, B. Williams, Q. Qin, A. Lee, Q. Hu, and J. Reno, *Opt. Express*, **15**, 113–128 (2007).
90. A. Lee, B. Williams, S. Kumar, Q. Hu, and J. Reno, *Opt. Lett.*, **35**, 910–912 (2010).
91. C. Pflugl, M. Belkin, Q. Wang, M. Geiser, A. Belyanin, M. Fischer, A. Wittmann, J. Faist, and F. Capasso, *Appl. Phys. Lett.*, **93**, 161110-3 (2008).
92. T. Bartel, P. Gaal, K. Reimann, M. Woerner, and T. Elsaesser, *Opt. Lett.*, **30**, 2805–2807 (2005).
93. J. Dai, X. Guo, and X.-C. Zhang, *Technologies for Homeland and Security*, HST'09 IEEE, Conference, Boston (2009), pp. 453–456.
94. J. Dai, X. Lu, J. Liu, I. Ho, N. Karpowicz, and X.-C. Zhang, *Terahertz Sci. Technol.*, **2**, 131–143 (2009).
95. T.-J. Wang, S. Yuan, Y. Chen, J.-F. Daigle, C. Marceau, F. Theberge, M. Chateauneuf, J. Dubois, and S. Chin, *Appl. Phys. Lett.*, **97**, 111108-3 (2010).
96. Y. Zhang, Y. Chen, C. Marceau, W. Liu, Z.-D. Sun, S. Xu, F. Theberge, M. Chateauneuf, J. Dubois, and S. Chin, *Opt. Express*, **16**, 15483–15488 (2008).
97. S. Xu, Y. Zhang, Y. Zheng, and W. Liu, *Terahertz Sci. Technol.*, **3**, 130–142 (2010).
98. W. Withayachumnankul, G. M. Png, X. X. Yin, S. Atakaramians, I. Jones, H. Lin, B. Ung, J. Balakrishnan, B. W.-H. Ng, B. Ferguson, S. P. Mickan, B. M. Fischer, and D. Abbott, *Proc. IEEE*, **95**, No. 8, 1528–1558 (2007).
99. J. Dai, X. Xie, and X.-C. Zhang, *Phys. Rev. Lett.*, **97**, 103903-4 (2006).
100. M. C. Nuss and J. Orenstein, in: *Topics in Applied Physics*, Vol. 74, *Millimeter and Submillimeter Wave Spectroscopy of Solids*, Springer-Verlag, Berlin, Heidelberg (1998), pp. 7–50.
101. R. Smith and M. Arnold, *Appl. Spectrosc. Rev.*, **46**, 636–679 (2011).
102. S. Nishizawa, K. Sakai, N. Hangyo, T. Nagashima, M. W. Takeda, K. Tominaga, A. Oka, K. Tanaka, and O. Morikawa, in: *Topics in Applied Physics*, Vol. 97, *Terahertz Optoelectronics*, K. Sakai (Ed.), Springer-Verlag, Berlin, Heidelberg (2005), pp. 203–270.
103. G. Kitaeva, *Laser Phys. Lett.*, **5**, 561–564 (2008).

104. M. Naftaly and R. Dudley, *Opt. Lett.*, **34**, 1213–1215 (2009).
105. http://lts.fzu.cz/en/intro.htm [Online; Accessed Jun. 30, 2012].
106. S. Vidal, J. Degert, M. Tondusson, J. Oberle, and E. Freysz, *Appl. Phys. Lett.*, **98**, 191103-3 (2011).
107. X. Wang, Y. Cui, W. Sun, J. Ye, and Y. Zhang, *J. Opt. Soc. Am. A*, **27**, 2387–2393 (2010).
108. A. Jameson, "*Generating and Using Terahertz Radiation to Explore Carrier Dynamics of Semiconductor and Metal Nanostructures*," Ph.D. Thesis, Oregon St. Univ. (2012).
109. P. Jepsen and B. Fischer, *Opt. Lett.*, **30**, 29–31 (2005).
110. N. Karpowicz, D. Jianming, L. Xiaofei, Y. Chen, M. Yamaguchi, H. Zhao, X.-C. Zhang, M. Price-Gallagher, C. Fletcher, O. Mamer, A. Lesimple, and K. Johnson, *Appl. Phys. Lett.*, **92**, 011131-3 (2008).
111. K. Yamamoto, M. Yamaguchi, F. Miyamaru, M. Tani, M. Hangyo, T. Ikeda, A. Matsushita, K. Koide, M. Tatsuno, and Y. Minami, *Jpn. J. Appl. Phys.*, **43**, 414–417 (2004).
112. J. Barber, D. E. Hooks, D. J. Funk, R. D. Averitt, A. J. Taylor, and D. Babikov, *J. Phys. Chem. A*, **109**, 3501–3505 (2005).
113. N. Palka, T. Trzcinski, and M. Szustakowski, *Acta Phys. Pol., A*, **122**, No. 5, 946–949 (2012).
114. M. Leahy-Hoppa, M. Fitch, X. Zheng, L. Hayden, and R. Osiander, *Chem. Phys. Lett.*, **434**, 227–230 (2007).
115. M. Hangyo, M. Tani, and T. Nagashima, *J. Infrared, Millimeter, Terahertz Waves*, **26**, 1661–1690 (2005).
116. H.-T. Chen, W. J. Padilla, J. M. O. Zide, A. C. Gossard, A. J. Taylor, and R. D. Averitt, *Nature*, **444**, 597–600 (2006).
117. M. M. Nazarov, A. A. Angeluts, D. A. Sapozhnikov, and A. P. Shkurinov, *Izv. Vyssh. Uchebn. Zaved., Radiofiz.*, **52**, No. 8, 595–606 (2009).
118. J. Baxter and G. Guglietta, *Anal. Chem.*, **83**, No. 12, 4342–4368 (2011).
119. M. Scheller and M. Koch, *Opt. Express*, **17**, 17723–17733 (2009).
120. N. Krumbholz, C. Jansen, M. Scheller, T. Muller-Wirts, S. Lubbecke, R. Holzwarth, R. Scheunemann, R. Wilk, B. Sartorius, H. Roehle, D. Stanze, J. Beckmann, L. S. von Chrzanowski, U. Ewert, and M. Koch, *Proc. SPIE Int. Soc. Opt. Eng.*, **7485**, 7485-04 (2009).
121. W. Tribe, D. Newnham, P. Taday, and M. Kemp, *Proc. SPIE Int. Soc. Opt. Eng.*, **5354**, 168–176 (2004).
122. P. Benicewicz, J. Roberts, and A. Taylor, *J. Opt. Soc. Am.*, **12**, 2533–2546 (1994).
123. N. Sarukura, H. Ohtake, S. Izumida, and Z. Liu, *J. Appl. Phys.*, **84**, 654–666 (1998).
124. M. Li and X. Zhang, *Proc. SPIE Int. Soc. Opt. Eng.*, **3616**, 126–135 (1999).
125. A. Gurtler, C. Winnewisser, H. Helm, and P. Jepsen, *J. Opt. Soc. Am.*, **1**, 74–83 (2000).
126. S. Izumida, S. Ono, Z. Liu, H. Ohatake, and N. Sarukura, *Appl. Phys. Lett.*, **75**, 451–453 (1999).
127. T. Kondo, M. Sakamoto, M. Tonouchi, and M. Hangyo, *Jpn. J. Appl. Phys.*, **38**, L1035–L1037 (1999).
128. M. Kemp, A. Glauser, and C. Baker, *Proc. SPIE Int. Soc. Opt. Eng.*, **6212**, 62120T-6 (2006).
129. Y. Shen, P. Taday, and M. Kemp, *Proc. SPIE Int. Soc. Opt. Eng.*, **5619**, 82–89 (2004).
130. Y. Shen, P. Taday, D. Newnham, and H. Pepper, *Semicond. Sci. Technol.*, **20**, S254–S257 (2005).
131. P. Jepsen, D. Cooke, and M. Koch, *Laser Photonics Rev.*, **5**, 124–166 (2011).
132. M. Kemp, *Terahertz Sci. Technol.*, **1**, 282–292 (2011).
133. V. Krozer, T. Loffer, J. Dall, A, Kusk, F. Eichan, R. Olsson, J. Buron, P. Jepsen, V. Zhurbenko, and T. Jensen, *IEEE Trans. Microwave Theory Tech.*, **58**, 2027–2039 (2010).
134. F. Simoens, J. Meilham, B. Delplanque, S. Gidon, G. Lasfarques, J. Lalanue Dera, D. Nguyen, J. Ouvrier-Buffet, S. Pocas, T. Mailon, O. Cathhaband, and S. Barbieri, *Proc. SPIE Int. Soc. Opt. Eng.*, **8363**, 8363D-1–5 (2012).
135. H. Zhong, A. Redo-Sanchez, and X.-C. Zhang, *Opt. Express*, **14**, 9130–9141 (2006).
136. Z. Zhang, Y. Zhang, G. Zhao, and C. Zhang, *Optik*, **118**, 325–329 (2007).
137. C. Konek, B. Mason, J. Hooper, C. Stoltz, and J. Wilkinson, *Chem. Phys. Lett.*, **489**, 48–53 (2010).
138. H. Zhong, A. Redo-Sanchez, and X.-C. Zhang, *Int. J. High Speed Electron. Syst.*, **17**, 239–249 (2007).
139. Y. Watanabe, K. Kawase, and T. Ikari, *Appl. Phys. Lett.*, **83**, 800–802 (2003).
140. Y. Watanabe, K. Kawase, T. Ikari, H. Ito, Y. Ishikawa, and H. Minamide, *Opt. Commun.*, **234**, 125–129 (2004).
141. C. Baker, W. Tribe, T. Lo, B. Cole, S. Chandler, and M. Kemp, *Proc. SPIE Int. Soc. Opt. Eng.*, **95**, 1559–1565 (2007).
142. T. Lo, I. Gregory, C. Baker, P. Taday, W. Tribe, and M. Kemp, *Vib. Spectrosc.*, **42**, 243–248 (2006).
143. H.-B. Liu, Y. Chen, G. Bastiaans, and X.-C. Zhang, *Opt. Express*, **14**, 415–423 (2006).

144. H. Zhong, *"Terahertz Wave Reflective Sensing and Imaging,"* Doctoral dissertation, Rensselaer Polytechnic Inst. (2006).
145. Y. C. Shen, T. Lo, P. F. Taday, B. E. Cole, W. R. Tribe, and M. C. Kemp, *Appl. Phys. Lett.*, **86**, 241116-3 (2005).
146. M. Brandstetter, C. Deutsch, M. Krall, H. Detz, D. C. MacFarland, T. Zederbauer, A. M. Andrews, W. Schrenk, G. Strasser, and K. Unterrainer, *Appl. Phys. Lett.*, **103**, 17113-5 (2013).
147. J. Federici, B. Schulkin, F. Huang, D. Gary, R. Barat, F. Oliveiraand, and D. Zimdars, *Semicond. Sci. Technol.*, **20**, S266–S280 (2005).
148. A. W. M. Lee, Q. Qin, S. Kumar, B. S. Williams, Q. Hu, and J. L. Reno, *Appl. Phys. Lett.*, **89**, 141125-3 (2006).
149. A. Lee, B. Williams, S. Kumar, Q. Hu, and J. Reno, *IEEE Photonics Technol. Lett.*, **18**, 1415–1417 (2006).
150. Q. Hu, *Terahertz Sci. Technol.*, **1**, 1–10 (2008).
151. N. Oda, *C. R. Phys.*, **11**, 496–509 (2010).
152. N. Oda, A. Lee, T. Ishi, I. Hosako, and Q. Hu, *Proc. SPIE Int. Soc. Opt. Eng.*, **8363**, 83630A-5 (2012).